A first principles investigation of activation and dissociation of CO_2 on α-Fe_2O_3 (0001) surface.

Touko Lehenkari
2504313
Master's Thesis
Supervisor: Assa Aravindh Sasikala Devi
Co-Supervisor: Matti Alatalo
Unit: Nano and molecular systems research unit
Faculty: Faculty of Science
University of Oulu
Autumn 2021

Contents

1 Preface

Climate change is the most dire existential crisis being faced by the planet earth. A century of fossil fuel dependent economy has filled the air with carbon dioxide, raising the temperatures annually. As this new decade has come to pass, so have the many of the disastrous effects of the changed climate. The solution to the problem is twofold: invention of new carbon neutral ways to produce sustainable energy, or convert the greenhouse gasses already on our atmosphere into useful fuels. The goal of this thesis is to aid in both.

CO_2 is the main greenhouse gas causing climate change and the end product of every traditional combustion engine. It also composes 95% of the Martian atmosphere, making the reduction of it critical for terraforming. However, CO_2 is notoriously stable, both due to its straight geometry and strong bonds. Different reduction and conversion methods are therefore constantly being developed. The research is focused on materials that can activate CO_2 as possible catalysts to aid in reactions synthesis of CO_2 into useful products [17]. The activation can range from bending to splitting to ionizing the molecule leading to reduced activation barriers in chemical processes. New methods based on new catalyst materials could help close the broken carbon cycle. The search for new materials or compounds capable of activating CO_2 is ongoing and this thesis is part of the effort.

Hematite (figure 1), or more specifically α-Fe_2O_3 is the most stable ferric oxide. It is so prevalent, that it is the main ore used in steel production industry. In layman's terms its is known simply as rust. Why is hematite the material of interest in this thesis? Despite its wide availability and seemingly mundane outlook, hematite has been studied intensively for the past two decades. The band gap of hematite has experimentally been determined to be in between 1.9-2.2 eV, which is sufficient for photoexcitations to occur on its surface under a light source. This has motivated vast scientific inquiries to split water under sunlight for hydrogen production. Hematite can reach a theoretical maximum of 15% solar to hydrogen efficiency, passing the 10% benchmark required for practical applications [2]. The story of hematite might not end in a blast furnace or on a side of an abandoned cruise ship, but might keep on evolving.

Given these photocatalytically desirable properties, the morphologies, performance with cocatalysts and heterojunctions have been widely researched. Perhaps this knowledge can be of use for other applications as well. Maybe on splitting other molecules such as CO_2? Hematite is also stable in water, making important aqueous reduction applications possible. Finally a recent computational study has suggested hematite to be a good candidate for reduction of CO_2 [24]. The interaction between CO_2 and hematite has not been properly studied, and this thesis will make one of the first inquiries to the topic.

More specifically, this thesis is a first principles computational density functional theory (DFT) study on hematite's capabilities to activate and dissociate carbon dioxide with aiding dopants; manganese (Mn) and Cobalt (Co). It also contains a literature review, for this subject has not yet been thoroughly studied and therefore leaves some room for speculation. The literature review will also aid in comparing the results of the study and the choice of dopants.

Figure 1: Photo of a hematite ore [65]. The α-phase of Fe_2O_3 can be identified with the rust red streak marked with the red circle.

2 Literature review

2.1 CO_2 reduction

In this literature review, the activation and reduction of CO_2 is studied in a variety of materials. The goal is to shed light on the recent progress on the reactivity of CO_2 with different catalysts and find common trends in the initial activation of CO_2.

Franco et al. [17] reviewed the role of transition metals in the catalytic reduction of CO_2. Transition metals have been widely studied in this regard in the recent past and many methods have been proposed ranging from molecular catalysts and metal nanoparticles to bulk heterogeneous materials. In molecular catalysts, a transition metal particle is surrounded by a specific organic ligand framework to form a desired active state for the activation of CO_2. The size and surface structure of metal nanoparticles are scalable factors for their catalytic performance, and this tunability makes them interesting candidates.

Bulk heterogenous materials such as doped metal surfaces contain a large number of poorly characterised active sites. The effectiveness of this traditional approach has been challenged by single atom catalysts. Single atom catalysts are single transition metal atoms placed on 2D conductive surfaces. The singular atoms on the surfaces have

less options for migrating in to different positions and therefore the formed active sites are similar. In the moment of writing this review, the single particle method seems to outperform the bulk method. This suggests that transition metal catalysts containing well defined active sites might be more active towards CO_2 conversion and with better selectivity.

Effective steps have been taken in the field for future practical applications. As the activation and selectivity of CO_2 conversion still vary widely given different catalyst sites, the field is still relatively young and much remains to be understood. Lessons from different fields of study might complement each other greatly and this review strongly suggests an interdisciplinary approach. The superior performances of single-atom catalysts (SACs) and the structural similarity with their molecular analogs, suggest that transition metal catalysts containing well-defined sites may be intrinsically more active and selective towards CO2 conversion than the bulk heterogeneous materials.

Copper (Cu) is one of the widely researched metals focussing on CO_2 reduction. Zhao et al. [4] reviewed the recent progress of Cu based heterogenous electrocatalysts. The problems still faced by Cu are the large overpotential for CO_2 activation and low selectivity for reduction products. Progress on selectivity has mainly been made in single- and double carbon products, whereas the yield for larger carbon based molecule products has remained relatively low. Numerous different morphologies have been studied in order to improve the activity on Cu based electrodes. Regarding Cu, the most observed mechanisms agree that the first step in CO_2 reduction paths is the adsorption/activation of the CO_2 molecule. Cu also has photoelectronic applications and simple Cu(II)/Cu(0) has been demonstrated to host both CO_2 reduction and H_2O splitting in neutral aqueous solution with a H-type cell [5]. The review finally provides a comprehensive list of electrocatalysts that have been used thus far for these applications.

Recently a new record for high energy efficiency cathodic electroreduction of CO_2 to CO using an electrolytic cell was set by Menga et al. [3] The study used a new anode material to speed up its oxygen evolution reaction (OER) of water to O_2. The new material was nickel–iron hydroxide carbonate (NiFe-HC) which showed superior activity to previous record holders such as IrO_2 and Pt. The study shows that the usage of low cost metals for the reduction of CO_2 is possible and preferable to costly noble metals.

Boutin and Robert [6] reviewed the molecular structures found in literature that were successful in the reduction of CO_2. The paper provides a comprehensive list of compounds that have been reported to electrochemically break down CO_2 or synthesize its products into more useful chemicals that could potentially be used as fuel. The main advantage in pursuing molecular catalysts over the usage of metal electrodes is their selectivity as they could potentially form the desired product more consistently. This is attributed to the well defined adsorption sites [17].

Kovačič et al. [23] reviewed ab initio research done on the photocatalytic reduction of CO_2 and compared their results with experimental results. Qualifying properties for

successful photocatalyst were favorable band gap, charge separation, and charge transfer. The minimum energy of the conduction band must be lower than the CO_2 reduction potential for the reduction mechanism in question to occur. The excitation state should also last as long as possible to increase the probability of contact with CO_2. The interaction of the catalyst with CO_2 should be optimal; not too weak nor strong. Weak interaction leads to inactivity and too strong will often lead to the decay of the catalyst.

The most researched materials are metal oxides such as TiO_2, MgO, Ga_2O_3, Bi_2MoO_6, In_2O_3 and Ta_2O_5. Catalysts are tuned by doping (with metals such as Pt, Cu, Cr, Ru, Pd, Ag, Fe, Co, and Ni), with defects or using catalysts. Z-scheme catalysts also hold promise. Z-scheme catalysts are made of two photocatalytically active semiconductors and exploit the high conduction band of one and the low valence band of another. The basic idea is to form a ladder of energy levels for the photoexcited electrons. Theoretical studies swiftly produce results on conduction and valence bands, band gap, and adsorption energies. Therefore they can be used to effectively screen for new catalytic surfaces for experimental engineering. This thesis is also a part of this ongoing screening process.

Kumar et al. [24] modeled CO_2 reduction on hematite surfaces by the means of DFT calculations. The study systematically considered 139 possible reaction mechanisms with 20 intermediates and 63 distinct elementary reaction steps with hydrogen, carbon and oxygen products. Methanol was found to be the most favoured end product.

The initial activation of CO_2 begins with CO_2 binding onto the clean surface with bent geometry. Both iron and oxygen act as binding sites for CO_2 with oxygen favouring to bond with CO_2:s iron and carbon with oxygen. The splitting of the CO_2 afterwards occurs endothermically. Another exothermic reaction of CO_2 splitting was found with surface bound COOH intermediate. The study highly encourages more studies on hematite for the reduction of CO_2.

Chemisorption and dissociation of CO_2 was investigated on Ni[110] surface by the means of first principles calculations by Czelej et al [25]. The decomposition to CO and O was found to be favorable in all the cases calculated. In all the cases CO_2 first diffused into the surface before dissociating. It should be noted that the position of CO_2 was always the same leading up to the breaking of the C=O bond, no matter where the molecule was placed initially. The CO_2 molecule exhibits a significant reduction in the O–C–O angle, this is related to the charge transfer from the metal surface to the molecule. Similar bent geometry was also noted earlier in hematite by Kumar et al. [24].
A recent study investigated the interaction between the hexagonal ω phase of iron with carbon dioxide. In this first principles study by Aravindh et al. [52] multiple CO_2 configurations were put on an ω-Fe(0001) surface slab leading to physisorbtion, chemisorbtion and even to the splitting of the molecule. The most favourable adsorption energy was that of the horizontally chemisorbed CO_2. In this configuration a significant bend and elongation of the bonds was present.

A Bader charge analysis confirmed a notable charge transfer from the d-orbitals of Fe to the p-orbitals of O, which might explain the activation mechanism of the molecule leading into a spontaneous splitting of the CO_2 molecule.

An experimental study by Favaro et al. [20] used X-ray photon spectroscopy to investigate CO_2 reduction on a Cu(111) surface in the presence of water. A layer of oxygen below the Cu surface was found to be an essential requirement for CO_2 reduction. Water also played a crucial role, stabilizing the already physisorbed CO_2 and driving this state into a chemisorbed one, which in turn promotes CO_2 reduction further.

In a first principles study by Bernstein et al. [26] the disparency of the experimental and theoretical data of CO_2 reduction on Fe(100) surface was investigated. Theoretically speaking Fe should be a sufficient catalyst for the reduction of CO_2 but experimentally this has been observed not to be the case.

The study analysed the energetics of different reaction paths by a simplistic DFT based free energy approach and proposed the main limiting factor for CO_2 reduction; the preference of the absorbed C to form iron carbide (FeC_x). The formed iron carbide on the surface of Fe possesses rather different properties from the original material and CO_2 reduction didn't occur. This might explain the experimental findings.

A DFT+U study by Mishra et al. [55] investigated the activation of CO_2 on different CuO surfaces. The most stable exothermic configuration of CuO (011) surface closely resembles the bent configuration observed in this thesis. Also, the Bader charge analysis provides similar results of charge transfer of $-0.20e$ for that structure. The charge density difference is also strikingly similar with virtually the same orbital shape changes. Nano structures made of CuO have been intensively studied as a possible materials for CO_2 electroreduction [4].

In a slightly older DFT study by Cao et al. [56], CO_2 dissociation energies on a nickel (211) surface was investigated. The study achieved the same bent configurations as in this thesis but with smaller adsorption energies of >1 eV. The more interesting thing to note, however, is the linear correlation between the required dissociation energy and charge transfer. The more the surface donates charge to CO_2, the smaller the energy required for dissociation.

A scanning tunneling microscopy study by Lee et al. [57] investigated TiO_2 surface with an oxygen vacancy point defect. CO_2 molecule adsorped into the surface, filling the vacancy with its oxygen. The adsorbed molecule was then exited by injecting it with an electron. This caused the dissociation of CO_2 into a CO^- ion and a healed vacancy free surface. The threshold energy required for the dissociation in this manner was reported to be 1.4eV. The study concluded the formation of the transient CO^- ion to be the key process in CO_2 splitting. This study opens up the idea of the use of oxygen vacancies as a possible reaction site for CO_2 splitting for further study. Unfortunately irreversible processes such as this are not so desirable for catalytic applications due to the corrosion of the catalyst.

Liu et at. [58] conducted a DFT study on CO_2 activation and dissociation on low index transition metal surfaces. The Fe surface (100) yielded the most negative adsorption energy along with the biggest Bader charge difference. A correlation between the two was established. The more the surface donated negative charge to CO_2, the more favourable was the adsorption energy. In this case, the adsorbed configuration was bent and had accepted a charge of -1.36$|e|$ ionizing the CO_2.

Also CO and O were relaxed to the surfaces and the resulting stable adsorption geometries were used as a final states when calculating the dissociation energy barriers and reaction energies with the climbing image nudged elastic band method. The initial state was the stable adsorbed CO_2 in each case. It was shown that the lower reaction barrier for CO_2 dissociation occurs on Fe (110) surface. This result shows that higher adsorption energy and charge transfer do not always indicate favourable results for CO_2 dissociation.

Santos-Carballal et al. [59] investigated (001) and (111) surfaces of magnetite (Fe_3O_4), greigite (Fe_3S_4) and mackinawite (FeS) for possible CO_2 adsorption and dissociation. Magnetite and mackinawite materials successfully adsorbed CO_2 with magnetite having the largest adsorption energy, therefore having thermodynamically most probable adsorption. In magnetite, a trend between charge transferred from the surface to the CO_2 and adsorption energy was established. The study suggested that charge transfer is the cause for the bending of CO_2 to 130 degrees upon adsorption. In this configuration, a weakening of the C=O bond was identified with vibrational analysis. The CO_2 dissociation was studied using the climbing image nudged elastic band method to acquire activation energies and reaction paths. It was shown, that the only surface capable of dissociating CO_2 spontaneously was the mackinawite (111) surface due to electron donated by sulfur atoms to activate the adsorped CO_2 molecule.

2.2 Fe_2O_3 doping

Transition metal oxides such as hematite have been rigorously studied after the discovery of photo catalytic properties of TiO_2 by Fujishima and Honda in 1972 [9]. By doping, TiO_2:s enhanced photo catalytic properties have been achieved for the splitting of water as well as for the reduction of CO_2. As hematite has not yet widely been considered as a possible candidate for CO_2 reduction, the possibility of doping and improving its capabilities provides opportunities for further research. However, the water photoelectronic splitting reaction widely observed in hematite has been investigated with additional dopants. In this section, dopants and their influence on the photocataltic properties of Hematite is reviewed in the existing literature, searching for results to positively affect possible CO_2 reduction.
In a theoretical study by Congxin Xia et al. [7]the band gap of hematite with added sulfur defects was investigated using DFT and found that the band gap of α-hematite can easily be adjusted with added S. Using S concentration of 5,6% the band gap is changed from 2.1 eV to 1.45 eV. This is an ideal value for the absorption of natural light and hematite with S doping is proposed to be a good material for photoelectric applications such as

the production of low cost solar-cells.

In a study by Yichun Yin et al. [8] hematite was doped using transition metals (V, Cr, Mn, Zn, Co, Ni, Cu, Nb, Mo, Ti) to fine-tune its electric properties for oxygen evolution reaction. Nanoparticles of hematite were doped using a molten-salt flux method and their structural- and electrochemical properties were systematically determined by multiple spectroscopic investigations. The change in band gap by the dopants remained under 0.1 eV in all cases, the largest reduction in the band gap was with Mn. Almost all the dopants increased the charge carrier density and therefore, improved the electrical conductivity of the nanoparticles, Co was the most efficient at the reduction of the oxygen evolution reaction overpotential (by 0.16 V).

Zhang et al. [10] investigated the effects of Cu ion doping in hematite by means of X-ray photoelectron spectroscopy. The study found that the oxidation number of the used Cu ions had a major effect on the electrochemical performance of the material. Cu^{+} doped hematite samples demonstrated increased performance as Cu^{2+} ions had the opposite effect leading to a formation of an inactive surface with a deteriorated electrochemical perfomance. Both ions led to complex changes in the surface.

Zinc (Zn) was used to dope hematite using the sol-gel method in a study by Saman et al. [11] The added Zn decreased the band gap down to 0.35 eV at 4% Zn and increased with the further addition of Zn. The photocatalytic activity of the doped hematite particles was studied by measuring their ability to break down rose bengal dye under UV light source. The particles with 4% Zn degraded the dye the fastest suggesting that this concentration will yield the best results for photoelectric applications.

Ahmad et al. [12] studied the morphology of pure and tin (Sn) doped hematite using field emission scanning electron microscopy and X-ray diffraction. Optical properties of the samples were studied by ultraviolet visible spectroscopy. The dopant concentrations in the study ranged from 0.5-3.0%. Zn increased the absorption of light at longer wavelengths as well as transmittance at smaller wavelengths therefore improving the electronic properties of hematite for sensor elements.

Hematite was doped with titanium (Ti) in an experimental study by Nikolić et al. [13] XRD, SEM and EDS analyses indicated that Ti had an excellent solubility at 5% to 10% (wt. TiO_2) when pseudobrookite (Fe_2TiO_5) started to form as indicated by SEM and EDS analyses. In the latter case, the conductivity of grain boundaries was substantially increased. The increased conductivity was due to increased electron hopping between Fe^{2+} and Fe^{3+} enhanced by Ti substitution.

Chemelewsk et al. [14] studied thin hematite films under oxygen ambient conditions simulated solar irradiation and doped by silicon (Si). Si prefers to segregate to the surface of hematite, does not improve the conductivity in the bulk and lowers the optical adsorption coefficient. However in the case of a porous film the photoelectrochemical

performance was increased by the addition of Si due to its ability to aid charge transfer to the solution. Also the spectral response remains unchanged by the addition of Si.

Samanta et al. [15] studied the electro catalytic performance of Nickel (Ni) doped hematite nanoclaws. The nanoclaws demonstrated superb elecrocatalytic activity under a light source with a low overpotential for oxygen evolution reaction, being more effective than most state-of-the-art electrocatalysts. The unique morphology of the nanoclaws exposed a lot of active sites and the Ni dopant vastly increased their quantity.

Fe(100) and Fe_5C_2 surfaces were doped with first row transition metals (Mn, Cu, Cr, Ni Co) in a spin polarized DFT study by Gong et al. [16] Mn and Cr were found to be favourable for CO activation and dissociation while the other elements weren't favorable. A linear relationship with the electronegativity of the used element and its activation energy was established. Metals with lower electro negativity than Fe might donate electrons to doped sites and cause activation in CO with a delocalized 2p orbital of O.

The photoelectrochemical performance of hematite films doped with various metals was studied by Bak et al. [27]. Pt, Ce, Cd, Al, and Sn at 5% improved whereas Co, Ni, Cu and Ru at same amounts reduced the photoelectrochemical performance. In this study the important property that showed better performance was electrical conductivity. Pt and Cd were also reported to increase the band gap by 0.06eV whereas Cr decreased it by the same amount.

3 Theory

3.1 Schrödinger's equation of solid matter

Condensed matter is formed from closely packed atoms. This encompasses everything from liquids to solids to even neutron stars. These widely different forms of matter require different interpretations and the physics of condensed matter branches out to different fields of study. The most intensively studied field among these is the physics of the solid state. Solid state of matter is defined by its phase, excluding gaseous and liquid phases. The goal of solid state physics is to derive the observed properties of matter from its atomic scale physical phenomena. These phenomena are explained by the quantum mechanics of electrons under a potential formed by atomic cores.

Considering that the material has not been excited, the cores form a static potential for their electrons. We are essentially now studying a time independent system. The energy of this system is then a constant and its represented by its time independent Schrödinger's equation:

$$\hat{H} |\psi\rangle = E |\psi\rangle . \tag{3.1}$$

Let's now only consider the electrons in this system and make the Born-Oppenheimer approximation; that is the nuclei stay completely fixed. This is a reasonable, as the movements of the nuclei occur on an entirely different time scale than movement of the electrons. From a point of view of a rapidly fidgeting electron, the much heavier nucleus might as well not be moving at all.

The Hamiltonian operator $\hat{H}$ can then be separated into three parts: the total kinetic energy $\hat{T}$, total potential energy of the electrons $\hat{V}$ and the potential energy of the electrons interacting with the nuclei $\hat{V}_{ext}$. The last term is commonly referred to as the external potential and will be addressed as such. The equation reads:

$$\left(\hat{T} + \hat{V} + \hat{V}_{ext}\right) |\psi\rangle = E |\psi\rangle . \tag{3.2}$$

3.2 The exponential wall

The many body problem (3.2) poses a grand challenge via its shear complexity. Let's say that one tries to solve a many body wave function $|\psi\rangle$ of a molecule of n electrons using the variational principle. One begins with a trial function $|\psi\left(p_1, p_2, ...p_m\right)\rangle$, where $p_1, p_2, ...p_m$ are adjustable parameters. One then solves the schrödinger's equation for this trial function, changing the parameters until the properties of the system match with experimental data or its total energy reaches its minimum value; its ground state.

This straightforward method, whilst plausible in theory, has a fundamental problem with the storing of its information. Let's apply it to a molecule of n electrons while ignoring symmetries and spin. The number of parameters one has to use to represent one variable might vary, but let us settle on an average value of p. The number of required parameters m needed to represent the trial many body wave function when each electron has three spacial coordinates is then:

$$m = p^{3n}.$$

The space required to store the wave function grows exponentially with the addition of more electrons. So does the computational burden in a similar fashion. For even singular molecules, this variational- or any other method that requires the solving of the schrödinger's equation is far beyond of what any modern computers can handle. Therefore, modern computational methods in solid state physics do not depend on knowing the exact solution to the many body Schrödinger's equation.

3.3 Hohenberg-Kohn theorem

The Hohenberg-Kohn formulation [45] can be summarised by its basic lemma that states: *The ground-state density* $\tilde{n}(\mathbf{r})$ *of a bound system of interacting electrons in some external potential* $\hat{V}_{ext}(\mathbf{r})$ *determines this potential uniquely.*

In other words for any potential caused by the nuclei there exists a unique density of electrons corresponding to that potential. From electron density one can determine the potential and from the potential one can determine the density. Electron density $\tilde{n}(\mathbf{r})$ also determines the number of electrons N in the system. Recalling that $\hat{H} = \hat{T}(N) + \hat{V}(N) + \hat{V}_{ext}$, the electron density will also yield all properties that can be derived from its Hamiltonian. This is because electrons are completely identical particles and the differences in the systems are brought only from $\hat{V}_{ext}$. This is the basis of all modern density functional theory.

3.4 Self consistent Hartree equations

Now that the importance of electron density has been established, the next step is form a density to represent the system. This can be done iteratively with Hartree equations by calculating them in turns until the density is adjusted to desired accuracy.
One first begins with an initial guess for the density $n(\mathbf{r})$ and constructs an effective single-particle-potential $\hat{V}_H(\mathbf{r})$:

$$\hat{V}_H(\mathbf{r}) = -\frac{Z}{r} + \int \frac{n(\mathbf{r}')}{|\mathbf{r} - \mathbf{r}'|} d\mathbf{r}'. \tag{3.3}$$

The first potential acting on the electron is caused by a nucleus of atomic number Z and the latter potential by the average electron density distribution. Now (3.3) can be used to write the single particle Schrödinger equation for a single electron:

$$\left\{ -\frac{1}{2}\nabla^2 + \hat{V}_H(\mathbf{r}) \right\} \psi_j(\mathbf{r}) = \epsilon_j \psi_j(\mathbf{r}). \tag{3.4}$$

From here on, j is a short hand for all the quantum numbers; spacial as well as spin. The last step to end one iteration is to sum the single particle Schrödinger equations to a new mean electron density:

$$n(\mathbf{r}) = \sum_{j=1}^{N} |\psi_j(\mathbf{r})|^2 . \tag{3.5}$$

The most important property of the ground state density is its energy E_0. This can be extracted by using the Rayleigh-Ritz minimal principle:

$$E_0 = \min_{\psi} \langle \psi | \hat{H} | \psi \rangle . \tag{3.6}$$

Here ψ represents a normalized antisymmetric trial function for the given number of electrons N. The hamiltonian H is of the familiar form (3.2):

$$E_0 = \min_{\psi} \langle \psi | \hat{T} + \hat{V} + \hat{V}_{ext} | \psi \rangle .$$

The minimization of ψ can be separated into two steps. We have denoted $n(\mathbf{r}) \to n$ for notational beauty. First step minimizes ψ giving a density n and afterwards we perform the minimization over this n.

$$\begin{aligned} E_0 &= \min_{n} \min_{n \to \psi} \langle \psi | \hat{T} + \hat{V} + \hat{V}_{ext} | \psi \rangle . \\ &= \min_{n} \{ \min_{n \to \psi} \langle \psi | \hat{T} + \hat{V} | \psi \rangle + \min_{n \to \psi} \langle \psi | \hat{V}_{ext} | \psi \rangle \}. \\ &= \min_{n} \{ \min_{n \to \psi} \langle \psi | \hat{T} + \hat{V} | \psi \rangle + \int n \hat{V}_{ext} d^3\mathbf{r} \}. \end{aligned}$$

The former part is independent of the external potential $\hat{V}_{ext}$. For any system of N particles, this term is going to have the same form. It is called the universal functional $F[n]$.

$$F[n] = \min_{n \to \psi} \langle \psi | \hat{T} + \hat{V} | \psi \rangle . \tag{3.7}$$

The formulation of the minimal Rayleigh-Ritz principle in terms of trial densities n rather than the wave functions ψ in this way is called the constrained search method. It was proposed by Levy and Lieb in 1982. Finally the ground state energy expressed in this way is:

$$E_0 = \min_{n} \{ F[n] + \int n \hat{V}_{ext} d^3\mathbf{r} \}. \tag{3.8}$$

3.5 Kohn-Sham equations

After the Hartree equations were first used, a discrepancy was soon reported between their solutions and experimental data. The main reason Hartree equations tend to produce inaccurate results lies within the Hartree potential $V_H(\mathbf{r})$ (3.3). In reality, the electrons do not produce a consistent mean field due to them being quantum mechanically behaving fermions. Even as the particles are indistinguishable this mean field fails to abide by restrictions brought by the Pauli exclusion principle or the correlation effects the electrons have with one another for example.

The addition of quantum mechanical effects was included by Walter Kohn and Lu Sham in 1964 in their Kohn-Sham equations [46], forming a basis for modern density functional theory. They are self consistent and used similarly to Hartree equations by iterating to desired accuracy. Again, one begins with an initial guess for $n(\mathbf{r})$ and forming the effective potential:

$$\hat{V}_{eff}(\mathbf{r}) = \hat{V}_{ext}(\mathbf{r}) + \int \frac{n(\mathbf{r}')}{|\mathbf{r} - \mathbf{r}'|} d\mathbf{r}' + \hat{V}_{xc}(\mathbf{r}). \tag{3.9}$$

$\hat{V}_{ext}(\mathbf{r})$ is the potential caused by the atomic cores and the second term is the potential caused by the mean density similar to Hartree potential. The last term $\hat{V}_{xc}(\mathbf{r})$ includes the quantum mechanical effects as well as the self interaction that an electron has with itself in between iterations. $\hat{V}_{xc}(\mathbf{r})$ does not have a defined form and it is therefore approximated. It will be discussed in the next section.
With the effective potential the single particle equations $\phi_j(\mathbf{r})$, also known as *orbitals* can be solved as:

$$\left\{ -\frac{1}{2}\nabla^2 + \hat{V}_{eff}(\mathbf{r}) \right\} \phi_j(\mathbf{r}) = \epsilon_j \phi_j(\mathbf{r}). \tag{3.10}$$

An interesting thing to note here is that just like Hartree single particle equations (3.4) the wave functions ϕ_j and energies ϵ_j do not have observable meanings.
All of the quantum mechanical effects are included in the potential, leaving the electrons non interacting. Finally a new density $n(\mathbf{r})$ is formed by summing the single particle equations:

$$n(\mathbf{r}) = \sum_{j=1}^{N} |\phi_j(\mathbf{r})|^2 . \tag{3.11}$$

These three Kohn-Sham equations (3.9-11) are exact, meaning that one *can* produce the correct density for the system. The basic idea is to come to the same density as with interacting electrons by changing the effective potential. With some potential the density will be the same for noninteracting as it is with interacting electrons. Therefore we can get an exact answer as long as the exchange-correlation potential $V_{xc}(\mathbf{r})$ is correct.

As the single electron solutions are summed into electron density (3.11), an all electron wave function is not constructed as a part of this method. Still, the form of one is known as the all electron Kohn-Sham wavefunction Φ and it is a Slater determinant (appendix

7.1), constructed from the lowest energy solutions to (3.10). The electrons in the system obey the rules of noninteracting fermions. Returning to the problem of extracting the ground state energy E_0 from electron density $n(\mathbf{r}) \to n$, Kohn and Sham proposed a new form for the universal functional (3.8):

$$F[n] = T_s[n] + E_{Hxc}[n]. \tag{3.12}$$

$T_s[n]$ is the energy functional for noninteracting electrons:

$$T_s[n] = \min_{\Phi \to n} \langle \Phi | \hat{T} | \Phi \rangle = \langle \Phi[n] | \hat{T} | \Phi[n] \rangle .$$

This is also the definition of the all electron wave function Φ. They are a single Slater determinant that is acquired by minimizing its elements over some electron density n. Therefore, they are functionals of the density denoted by $|\Phi[n]\rangle$.
E_{Hxc} is the Hartree exchange-correlation energy:

$$E_{Hxc}[n] = \frac{1}{2} \int \frac{n(\mathbf{r}) n(\mathbf{r}')}{|\mathbf{r} - \mathbf{r}''|} d^3\mathbf{r} d^3\mathbf{r}' + E_{xc}[n]$$

The first therm is known as the Hartree energy. Its physical meaning is the electrostatic repulsion for the charge distribution. Like the exchange-correlation potential V_{xc} in the Kohn-Sham equations, the exchange- correlation energy $E_{xc}[n]$ will be expanded upon in the next section [3.6].
Using (3.12) as a definition of the universal functional the equation for the ground state energy (3.8) takes the form:

$$\begin{aligned} E_0 &= \min_n \{ F[n] + \int n \hat{V}_{ext} d^3\mathbf{r} \} \\ &= \min_n \{ \min_{\Phi \to n} \langle \Phi | \hat{T} | \Phi \rangle + E_{Hxc}[n] + \int n \hat{V}_{ext} d^3\mathbf{r} \} \end{aligned}$$

The density that minimizes $\langle \Phi | \hat{T} | \Phi \rangle$ is the same that minimizes $\int n V_{ext} d^3\mathbf{r}$. Therefore, we can write the latter using the same Slater determinant as the former. This gives:

$$E_0 = \min_n \{ \min_{\Phi \to n} \langle \Phi | \hat{T} | \Phi \rangle + E_{Hxc}[n] + \langle \Phi | \hat{V}_{ext} | \Phi \rangle \}$$

The exchange correlation functional can be written in the therms of the same Slater determinant:

$$E_0 = \min_n \min_{\Phi \to n} \{ \langle \Phi | \hat{T} + \hat{V}_{ext} | \Phi \rangle + E_{Hxc}[n_\Phi] \}$$

As everything is now a function of this one Slater determinant, we can just minimize over it directly:

$$E_0 = \min_{\Phi}\{\langle\Phi|\,\hat{T} + \hat{V}_{ext}\,|\Phi\rangle + E_{Hxc}[n_\Phi]\}$$

Minimizing with respect to Φ finally gives the ground state energy E_0 for the interacting system:

$$E_0 = T_s[n] + \int\ nV_{ext}d^3\mathbf{r} + \frac{1}{2}\int \frac{n(\mathbf{r})n(\mathbf{r}')}{|\mathbf{r}-\mathbf{r}''|}d^3\mathbf{r}d^3\mathbf{r}' + E_{xc}[n] \tag{3.13}$$

We can also write this using the energies of the non interacting electrons ϵ_j in the effective potential:

$$\begin{aligned}\sum_j \epsilon_j &= T_s[n] + \int n\hat{V}_{eff}d^3\mathbf{r} \\ &= T_s[n] + \int \frac{n(\mathbf{r})n(\mathbf{r}')}{|\mathbf{r}-\mathbf{r}''|}d^3\mathbf{r}d^3\mathbf{r}' + \int n\hat{V}_{xc}d^3\mathbf{r} + \int n\hat{V}_{ext}d^3\mathbf{r}\end{aligned} \tag{3.14}$$

Inserting the above to (3.14) we finally come to the most useful representation of the ground state energy of the interacting electrons in the Kohn-Sham formulation:

$$E_0 = \sum_j \epsilon_j - \frac{1}{2}\int \frac{n(\mathbf{r})n(\mathbf{r}')}{|\mathbf{r}-\mathbf{r}''|}d^3\mathbf{r}d^3\mathbf{r}' - \int n\hat{V}_{xc}d^3\mathbf{r} + E_{xc}[n] \tag{3.15}$$

3.6 Exchange correlation potential

Computational simplicity is a perk of the Kohn-Sham method. The electrons themselves do not interact with one another but are under an effective potential $\hat{V}_{eff}$ that will form an electron density, similar to what one would get with interacting electrons. The promise of Kohn-Sham formulation to realistically describe electrons by including quantum mechanical effects then is fulfilled within the exchange correlation potential $\hat{V}_{xc}$ in (3.9) and energy E_{xc} in (3.15). Electron - electron interaction in the Kohn-Sham method is between singular electrons with the electron density. Different types of electron densities will have different exchange correlation effects with the electrons. Therefore different implementations of approximating this interaction exist, and the choice between them is of utmost importance.

The only system for which the exchange correlation energy is *precisely* determined is the homogeneous electron gas. Using this as an approximation of the electron density led to the first and perhaps the most influential approximation: the local density approximation

(LDA). Being proposed by Kohn and Sham [46], LDA is the most simplistic approximation used for the exchange correlation energy, depending only on the given electron density. In LDA, the exchange correlation energy E_{xc}^{LDA} is approximated by the exchange correlation energy of a uniform electron gas of the given density per particle ϵ_{xc}^{unif}:

$$E_{xc}^{LDA} = \int n(\mathbf{r})\epsilon_{xc}^{unif}(n(\mathbf{r}))d^3\mathbf{r}. \tag{3.16}$$

Despite its simplicity, LDA has been reported to work rather well in solid systems and was is use for many years. Systems where the electron density varied smoothly and systems with only *sp*-bonds present produced correct results and increased scientific interest to the field of DFT. Still, its description of other types of atomic bonds was not sufficient and a tendency to over bind was widely reported. Some other notable well known limitations of LDA include systems where an independent particle picture brakes down. This lead to LDA categorising transition metal oxides (FeO, NiO & MnO) as semiconductors or metals when in reality they are all Mott insulators [53]. Even some simplistic bulk materials were falsely characterised by LDA. The most well know example of this is in the case of bulk iron, where LDA predicted a non-magnetic face centered cubic structure, when in reality iron has a strongly ferromagnetic body centered cubic structure [54].

The limitations of LDA became more apparent with its increased use. The discrepancy between LDA:s results and experimental data led to corrections being developed and tested. Notably, a type of gradient correction known as the generalized gradient approximation was reported to work well for metallic systems.

3.6.1 Generalized gradient approximation (GGA)

In this thesis we use generalized gradient approximation (GGA) for exchange correlation energy E_{xc}.
All GGA:s have a similar form of:

$$E_{xc}^{GGA}[n] = \int f(n(\mathbf{r}), \nabla n(\mathbf{r}))d^3\mathbf{r}. \tag{3.17}$$

Here f is yet an unknown function, dependent not only on the electron density n, but also its gradient ∇n. Within GGA, the most used implementation is the Perdew Burke Ernzerhof (PBE) GGA [35], that is also used in this thesis. The exchange-correlation energy in PBE is split into two parts:

$$E_{xc}^{GGA} = E_x^{PBE} + E_c^{PBE} \tag{3.18}$$

The exchange therm E_x represents the Pauli exclusion principle. As electrons are fermions their wavefunction is antisymmetric and cannot persist in the same space with another electron with same quantum number.

The correlation therm E_c contains the influence of all other electrons on the kinetic- and potential energies of one electron. These together make spaces with lesser density compared to non-interacting electrons known as exchange-correlation holes.

The PBE exchange energy has the form:

$$E_x^{PBE} = \int n(\mathbf{r})\epsilon_x^{unif}(n)F_x(s)d^3\mathbf{r},$$

where the exchange energy per particle of a uniform electron gas is $\epsilon_x^{unif}(n) = -3e^2k_F/4\pi$ and the enhancement function $F_x(s)$ is:

$$F_x(s) = 1 + 0.804 - \frac{0.804}{(1 + \frac{0.21951}{0.804}s^2).}$$

The final parameter s is given by the electron density and its gradient:

$$s = \frac{|\nabla n|}{2k_B n}.$$

Correlation energy in PBE is:

$$E_c^{PBE} = \int n(\mathbf{r})[\epsilon_c^{unif}(n) + H(r_s, t)]d^3\mathbf{r},$$

where $\epsilon_c^{unif}(n)$ is the single particle correlation energy. Its form varies in different conditions and is further explained by Perdew and Wang [36]. $H(r_s, t)$ is the enhanchement function now of the form:

$$H(r_s, t) = \frac{\beta^2}{2\alpha} ln\left[1 + \frac{2\alpha}{\beta}\frac{t^2 + At^4}{1 + At^2 + A^2t^4}\right].$$

A is defined as:

$$A = \frac{2\alpha}{\beta e^{[-2\alpha\epsilon_c^{unif}(n)]/\beta^2} - 1}.$$

Finally all the parameters are:

$$\alpha = 0.0716, \quad \beta = 0.066725, \quad t = \frac{|\nabla n|}{2k_s n} \;\&\; \quad k_s = \sqrt{\frac{4k_F}{\pi}}.$$

The basic idea in the PBE method is to use the energies per particle in a uniform electron gas and then apply an enhancement function to get the total exchange and correlation energies. The enhancement functions, also known as the gradient contributions and their constants were formulated by adjusting them to well known conditions of the exchange correlation begininning from ansatzes. The processes for both are expanded upon in more detail by Perdew et al. [35].

3.7 Plane wave basis

The form of single particle Kohn-Sham wave functions ϕ_j mentioned earlier in the section [3.5] representing the electrons in the system will be discussed in this section in detail. They should be accurate, yet mathematically simple enough for practical computations. Hematite is a periodic crystalline solid, composed of identical primitive cells (see section 4.1). It is therefore sufficient to only solve the electronic structure for one of these cells, when coming up with an electronic structure for the whole system. In a periodical solid, the electrons of each cell have same energies forming energy bands.

In this thesis, the plane wave method is used to represent how the single electron wave functions ϕ_j behave in a periodic potential created by the ions in the lattice. In accordance to Bloch's theorem [34], the electronic wave energy levels in a periodical solid takes the form of an energy band n that has a wave function that can be expressed as a combination of two components:

$$\phi_{n\mathbf{k}}(\mathbf{r}) = e^{i\mathbf{kr}} u_{n\mathbf{k}}(\mathbf{r}). \tag{3.19}$$

The former $e^{i\mathbf{kr}}$ is known as the plane wave part and latter the periodic cell part. $\mathbf{k}$ is known as the wave vector that is confined to the first Brillouin zone (see section 7.2). In this section, electrons are indicated with their band and their wave vector replacing $j \rightarrow (n\mathbf{k})$. The periodic cell part $u_{n\mathbf{k}}(\mathbf{r})$ is identical in every cell. It has the same periodicity as the structure, meaning that:

$$u_{n\mathbf{k}}(\mathbf{r} + \mathbf{R}) = u_{n\mathbf{k}}(\mathbf{r}),$$

where $\mathbf{R}$ is any of the lattice vectors. As $u_{n\mathbf{k}}(\mathbf{r})$ is cell periodical in this way, its discrete Fourier transform [7.2.1] only has contributions of the reciprocal lattice vectors denoted by $\mathbf{G}$:

$$u_{n\mathbf{k}}(\mathbf{r}) = \sum_{\mathbf{G}=0} c_{n\mathbf{k}}(\mathbf{G}) \frac{e^{i\mathbf{Gr}}}{\sqrt{\Omega}}.$$

$c_{n\mathbf{k}}(\mathbf{G})$:s are the plane wave expansion coefficients. In the normalization term $\Omega^{-\frac{1}{2}}$ the denominator Ω is the reciprocal primitive cell volume. The wave functions in DFT can be written as a linear combination of the plane waves:

$$\phi_{n\mathbf{k}}(\mathbf{r}) = \sum_{\mathbf{G}=0} c_{n(\mathbf{k}+\mathbf{G})} \frac{e^{i(\mathbf{k}+\mathbf{G})\mathbf{r}}}{\Omega}$$

$$\phi_{n\mathbf{k}}(\mathbf{r}) = \sum_{\mathbf{G}=0} c_{n(\mathbf{k}+\mathbf{G})} \zeta^{\mathbf{k}}_{\mathbf{G}}(\mathbf{r}). \tag{3.20}$$

Inside the first Brillouin zone, only some energy levels are allowed due to the quantum mechanical nature of the electrons. A bound quantum mechanical systems quantities only have discrete values with forbidden values between them. Therefore, for a defined value of the wave vector $\mathbf{k}$ aka a k-point in reciprocal space, there exists a set of finite energy

levels that this proposed sum of plane waves (3.20) can occupy. This means that even in an infinite system, only a finite set of electron wave functions needs to be calculated. However, given a continuous reciprocal space, the number of k-points is infinite, making the computational problem unsolvable. An approximation is then again in order. As it happens, one does not need to sum for the entirety of the reciprocal space in the first Brillouin zone, but for a selected finite set of k-points within it. This is due to electron wave functions being nearly identical with close values of $\mathbf{k}$.

The sum of reciprocal space vectors $\mathbf{G}$ in the electron wave functions (3.20) will be centered around the selected special k-points in the reciprocal space. They are summed until a specified cutoff energy:

$$E_{cut} \geq \frac{1}{2} |\mathbf{k} + \mathbf{G}|^2 . \tag{3.21}$$

Visualizing this in the reciprocal space yields special k-point centered spheres which encapsulate all the used wave vectors $|\mathbf{k} + \mathbf{G}|$.

3.7.1 Kohn-Sham equations with plane waves

In practical calculations with Kohn-Sham functions with any given basis, the single electron wave functions take the following form:

$$\sum_{\beta=1} \langle \psi_\alpha | \hat{H} | \psi_\beta \rangle c_{\beta i} = \epsilon_i \sum_{\beta=1} S_{\alpha\beta} c_{\beta i}. \tag{3.22}$$

On the left side $\langle \psi_\alpha | \hat{H} | \psi_\beta \rangle$ are the matrix elements of the electron Hamiltonian and $c_{\beta i}$ are their basis dependent coefficients. $S_{\alpha\beta}$ are the elements of the overlap matrix that defines the interactions of the basis and possible non orthogonality. Plane waves $\zeta^{\mathbf{k}}_{\mathbf{G}'}$ are orthogonal and therefore the overlap matrix takes the form of an identity matrix:

$$S^{\mathbf{k}}_{\mathbf{G},\mathbf{G}'} = \left\langle \zeta^{\mathbf{k}}_{\mathbf{G}} \middle| \zeta^{\mathbf{k}}_{\mathbf{G}'} \right\rangle = \delta_{\mathbf{G},\mathbf{G}'}$$

The elements are either 0 or 1 depending if $\mathbf{G}$ and $\mathbf{G}'$ are the same. Constructing the Hamiltonian $H = T + V$, the plane wave contribution to the kinetic energy is then:

$$\hat{T}^{\mathbf{k}}_{\mathbf{G},\mathbf{G}'} = -\frac{1}{2} \left\langle \zeta^{\mathbf{k}}_{\mathbf{G}} \middle| \nabla^2 \middle| \zeta^{\mathbf{k}}_{\mathbf{G}'} \right\rangle = \frac{1}{2} |\mathbf{k} + \mathbf{G}|^2 \delta_{\mathbf{G},\mathbf{G}'}$$

The contribution of potential energy is calculated similarly:

$$\hat{V}_{\mathbf{G},\mathbf{G}'} = \left\langle \zeta^{\mathbf{k}}_{\mathbf{G}} \middle| \hat{V}_{eff} \middle| \zeta^{\mathbf{k}}_{\mathbf{G}'} \right\rangle = \frac{1}{\Omega} \int_\Omega \hat{V}_{eff}(\mathbf{r}) e^{-i(\mathbf{G}-\mathbf{G}')} d^3\mathbf{r} = \hat{V}_{eff}(\mathbf{G} - \mathbf{G}').$$

$\hat{V}_{\mathbf{G},\mathbf{G}'}$ is local and independent of the wave vector $\mathbf{k}$. The integration over the primitive cell takes the form of the Fourier transform of the potential.
Finally the Kohn-Sham equations take the following form using the plane wave basis:

$$\sum_{\mathbf{G}'}[\frac{1}{2}|\mathbf{k}+\mathbf{G}|^2\delta_{\mathbf{G},\mathbf{G}'}+\hat{V}_{eff}(\mathbf{G}-\mathbf{G}')]c_{n\mathbf{k}}(\mathbf{G})=\epsilon_{n\mathbf{k}}c_{n\mathbf{k}}(\mathbf{G}), \tag{3.23}$$

where $\epsilon_{n\mathbf{k}}$ is the energy eigenvalue. The above can also be written more simply by using condensed matrix notation:

$$\mathbf{H}^{\mathbf{k}}\mathbf{c}^{\mathbf{k}}=\epsilon^{\mathbf{k}}\mathbf{c}^{\mathbf{k}}$$

The advantages of using plane waves in the Kohn-Sham method is the computational efficiency due to their orthogonality and ease of switching between the direct- and reciprocal spaces with fast Fourier transform. They are widely used in first principles calculations for solids.

3.8 Projector augmented wave method

The main disadvantage of the plane wave formalism is the interaction of electrons with atomic cores. In the immediate vicinity of a nuclei, plane waves have rapid oscillations due to their orthogonality. Describing these sharp features requires a huge cutoff energy (3.21) or a very dense special k-grid, both immensely increasing the computational cost.

A simple fix we will now make is a different description between core bound and valence electrons, known as the frozen core approximation. That is, core electrons will stay bound and their states remain unchanged when the atoms valence electrons are forming bonds. In each structure then, all the core states remain identical between atoms of same type. Even when using this approximation, the remaining valence electrons will still rapidly oscillate in the vicinity of a nucleus that is now screened by the core bound electrons. This still imposes a heavy computational load. The next fix is to change the description of the valence electrons themselves in the vicinity of a nucleus. This method is known as the projector augmented wave method (PAW) first proposed by Blöchl [41].

Let us begin by introducing two out of the three basis sets intrinsic to PAW. Firstly we have a set of one electron wave functions $\phi_{n\mathbf{k}}$; the real rapidly oscillating solutions to the Schrödinger equation near a nucleus. Secondly we have a set of pseudo one electron wave functions $\tilde{\phi}_{n\mathbf{k}}$ that are smooth projections of the one electrons wave functions around a nucleus. They both have the same eigenvalue spectrum. In PAW we can represent the one electron wave functions $\phi_{n\mathbf{k}}$ with pseudo wave functions $\tilde{\phi}_{n\mathbf{k}}$ inside a defined augmentation radius r_c forming a sphere around a nucleus using a transformation operator $\tilde{T}$:

$$|\phi_{n\mathbf{k}}\rangle=\tilde{T}\,|\tilde{\phi}_{n\mathbf{k}}\rangle\,,\mathbf{r}<r_c. \tag{3.24}$$

By their definition, outside of the augmentation sphere the pseudo and one electron wave functions are identical:

$$|\phi_{n\mathbf{k}}\rangle=|\tilde{\phi}_{n\mathbf{k}}\rangle\,,\mathbf{r}>r_c.$$

The form of $\tilde{T}$ is the following:

$$\tilde{T} = 1 + \sum_j (|\varphi_j\rangle - |\tilde{\varphi}_j\rangle) \langle \tilde{p}_j| \,. \tag{3.25}$$

$\tilde{p}_j$:s are projector functions; the third basis set of PAW along side the all electron - and pseudo wave functions. By their definition, they must be localised withing the augmentation region while also having the property:

$$\langle \tilde{p}_i | \tilde{\varphi}_j \rangle = \delta_{i,j}.$$

The use of projector functions is to examine the partial pseudo wave functions $|\tilde{\phi}_j\rangle$ when transforming them within $\tilde{T}$. Due to their orthogonality they define if the operation $+|\phi_j\rangle - |\tilde{\phi}_j\rangle$ is performed. The precise form and the method of constructing projection functions by iteratively otrhogonalizing with respect to the pseudo wave functions, are skipped in this thesis. An in depth example for those interested is included in [41] (section 6, part C).

Finally, $\phi_j(\mathbf{r})$ and $\tilde{\phi}_j(\mathbf{r})$ are the partial solutions to the radial schrödinger's equation around a nucleus of the one electron and pseudo wave functions, respectively. They are previously computed and supplemented by databases of first principle softwares. They are not expressed by plane waves but in radial logarithmic grids. Their forms are:

$$\phi_\alpha(\mathbf{r}) = \frac{1}{|\mathbf{r} - \mathbf{R}_\alpha|} u_{l_\alpha,\epsilon_\alpha}(|\mathbf{r} - \mathbf{R}_\alpha|) Y_{l_\alpha,m_\alpha}(\widehat{\mathbf{r} - \mathbf{R}_\alpha})$$

&

$$\tilde{\phi}_\alpha(\mathbf{r}) = \frac{1}{|\mathbf{r} - \mathbf{R}_\alpha|} \tilde{u}_{l_\alpha,\epsilon_\alpha}(|\mathbf{r} - \mathbf{R}_\alpha|) Y_{l_\alpha,m_\alpha}(\widehat{\mathbf{r} - \mathbf{R}_\alpha}).$$

The used index α signifies the atomic site $\mathbf{R}_\alpha$ with quantum numbers for angular momentum l_α, m_α and energy of ϵ_α. $u_{l_\alpha,\epsilon_\alpha}$ and $\tilde{u}_{l_\alpha,\epsilon_\alpha}$ are the radial components of the partial waves. Y_{l_α,m_α} is the component of spherical harmonics that only depends on the orientation of the $\mathbf{r} - \mathbf{R}_\alpha$ vector but not the length indicated by $\widehat{\ }$.
Now that the basis sets of PAW has been established, let us more closely observe the transformation (3.25) for more clarity on the basic working mechanism of PAW:

$$|\phi_{n\mathbf{k}}\rangle = |\tilde{\phi}_{n\mathbf{k}}\rangle - \sum_j |\tilde{\varphi}_j\rangle \langle \tilde{p}_j | \tilde{\phi}_{n\mathbf{k}}\rangle + \sum_j |\varphi_j\rangle \langle \tilde{p}_j | \tilde{\phi}_{n\mathbf{k}}\rangle \,.$$

The main idea behind the method is this: outside a specified region the wave function is represented by a pseudo wave function, but inside of the region, its components are replaced. First, the components of the pseudo wave function are cancelled out by partial waves $|\tilde{\varphi}_j\rangle$. After that, partial waves of the actual radial Schrödinger's equation $|\varphi_j\rangle$ are added to replace the pseudo partial waves lost.

The reason why so much computational effort was bypassed using this method is that the rapidly oscillating part of the real wave function is represented by a pre-calculated section, that is not being represented by plane waves. Therefore there is no need of a huge cutoff energy for the entire calculation outside the augmentation radius.

3.8.1 Energy using PAW-method

As the wave function in PAW, the energy functional can also be split into three parts. The following is the functional proposed by Kresse et al. [42] as that is the implementation used by the VASP software. The main difference between the Blöchl approach is in the arrangement of the terms for energy. The total energy term is:

$$E = \tilde{E} + E^1 - \tilde{E}^1. \tag{3.26}$$

Its constituents are:

$$\tilde{E} = \sum_n f_n \langle \tilde{\phi}_{n\mathbf{k}} | -\frac{1}{2}\nabla^2 | \tilde{\phi}_{n\mathbf{k}} \rangle + E_{xc}[\tilde{n}+\hat{n}+\tilde{n}_c] + E_H[\tilde{n}+\hat{n}] + \int v_H[\tilde{n}_{Zc}][\tilde{n}(\mathbf{r})+\hat{n}(\mathbf{r})]d\mathbf{r} + U(\mathbf{R}, Z_{ion}),$$

$$\tilde{E}^1 = \sum_{(i,j)} \rho_{(i,j)} \langle \tilde{\varphi}_i | -\frac{1}{2}\nabla^2 | \tilde{\varphi}_j \rangle + \overline{E_{xc}[\tilde{n}+\hat{n}+\tilde{n}_c]} + \overline{E_H[\tilde{n}^1+\hat{n}]} + \int_{\Omega_r} v_H[\tilde{n}_{Zc}][\tilde{n}^1(\mathbf{r})+\hat{n}(\mathbf{r})]d\mathbf{r}$$

&

$$E^1 = \sum_{(i,j)} \rho_{(i,j)} \langle \tilde{\varphi}_i | -\frac{1}{2}\nabla^2 | \tilde{\varphi}_j \rangle + \overline{E_{xc}[n^1+n_c]} + \overline{E_H[n^1]} + \int_{\Omega_r} v_H[\tilde{n}_{Zc}] n^1(\mathbf{r}) d\mathbf{r}.$$

Within these, the electrostatic potential v_H of a given charge density n is:

$$v_H[n] = \int \frac{n(\mathbf{r}')}{|\mathbf{r}-\mathbf{r}'|} d^3\mathbf{r}'.$$

The Hartree energy E_H for a given density n is:

$$E_H = \frac{1}{2} \int \int \frac{n(\mathbf{r}) n(\mathbf{r}')}{|\mathbf{r}-\mathbf{r}'|} d^3\mathbf{r}' d^3\mathbf{r}.$$

f_n are orbital occupation numbers, from which the occupancies of each augmentation channels ρ_{ij} can be calculated using the pseudo wave functions and projector functions:

$$\rho_{ij} = \sum_n f_n \langle \tilde{\phi}_{n\mathbf{k}} | \tilde{p}_i \rangle \langle \tilde{p}_j | \tilde{\phi}_{n\mathbf{k}} \rangle .$$

Lastly, the over lined therms $\overline{E}$ indicate that the given quantity is evaluated using a logarithmic radial grid within the augmentation region and $U(\mathbf{R}, Z_{ion})$ is the electrostatic energy of point like nuclei with charges of Z in a uniform electrostatic background.

3.8.2 Density using PAW-method

The electronic density terms, with which the energy functional of the last section was written are now explained. The valence electron density is split in three parts:

$$n(\mathbf{r}) = \tilde{n}(\mathbf{r}) + n^1(\mathbf{r}) - \tilde{n}^1(\mathbf{r}). \tag{3.27}$$

The softly varying pseudo charge density $\tilde{n}$ is calculated on a plane wave grid from the used pseudo wave functions as the basis:

$$\tilde{n}(\mathbf{r}) = \sum_n f_n \left\langle \phi_{n\mathbf{k}} | \mathbf{r} \right\rangle \left\langle \mathbf{r} | \phi_{n\mathbf{k}} \right\rangle .$$

The onsite charge densities are calculated on a localised logarithmic radial support grid using partial waves and occupancy terms:

$$n^1(\mathbf{r}) = \sum_{(i,j)} \rho_{ij} \left\langle \varphi_i | \mathbf{r} \right\rangle \left\langle \mathbf{r} | \varphi_j \right\rangle$$

&

$$\tilde{n}^1(\mathbf{r}) = \sum_{(i,j)} \rho_{ij} \left\langle \tilde{\varphi}_i | \mathbf{r} \right\rangle \left\langle \mathbf{r} | \tilde{\varphi}_j \right\rangle .$$

The charge density of the atomic core is made of two components. n_Z is the point charge density of a nucleus of charge Z and the density n_c of the core bound electrons in the frozen core approximation. They are summed into one term for notational clarity:

$$n_{Zn} = n_Z + n_c.$$

The same also holds for pseudo core densities $\tilde{n}_{Z/c}$. The total pseudo core density $\tilde{n}_{Zc}$ is equal to the ionic charge Z. They relate according to:

$$\int_{\Omega_r} n_{Zc}(\mathbf{r}) d^3\mathbf{r} = \int_{\Omega_r} \tilde{n}_{Zc}(\mathbf{r}) d\mathbf{r}.$$

The integration over Ω_r depicts an integration over the support radial grid.
The last density term $\hat{n}$ belongs to the compensation charge. The physical meaning of it is the correction of multipole moments of $\tilde{n}^1$ to match with n^1 by adding to the pseudo density. It is represented by a sum of center terms:

$$\hat{n} = \sum_{(i,j),L} \rho_{ij} \hat{Q}_{ij}^L(\mathbf{r}), \tag{3.28}$$

where Q:s are functions of the form:

$$\hat{Q}_{ij}^L(\mathbf{r}) = q_{ij}^L g_l(\mathbf{r} - \mathbf{R}) Y_L(\widehat{\mathbf{r} - \mathbf{R}}).$$

g_l are functions that normalize the momentum l to be equal to 1. The moment functions q_{ij}^L themselves are:

$$q_{ij}^{L} = \int_{\Sigma_r} Q_{ij}(\mathbf{r})|\mathbf{r}-\mathbf{R}|^{l} Y_L^*(\widehat{\mathbf{r}-\mathbf{R}})d\mathbf{r},$$

where L is used to notate the quantum numbers $L = (l, m)$.

3.9 Hubbard U correction

The generalized gradient approximation provides accurate results in ab initio studies of transition and rare earth metals and is widely used to this day. But as the list of studied transition metal materials came to encompass oxides or fluorides, some limitations of GGA became apparent. Ab initio studies of transition metal oxides wrongly predicted metallic ground state for many well reported Mott insulators such as CuO and FeO, by grossly underestimating their band gaps. The problem was reported in materials containing partly filled valence of d or f shells and its cause was quickly associated with inadequate description of Coulomb repulsion between localised electrons in those bands. These localised electrons are strongly correlated and have on-site quasi atomic interactions that can be described by the Hubbard U term:

$$U = E(d^{n+1}) + E(d^{n-1}) - 2E(d^{n}).$$

In this context, n is the site in an orbital d. The Hubbard U term is therefore defined as the energy required to place two electrons in the same location. Shifting an electron to a strongly correlated location from a weaker one will yield a considerable value for U. Ignoring this will cause errors of different magnitudes, depending on the localised electronic correlation on different electron sites. Indeed, the formation of transition metal oxides involves redox reactions in which electrons in the d band of the metal atoms are transferred to a vastly different environments of the oxygen atoms leading to a notable self interaction error.

The error can be revised by further modifying the exchange correlation energy term E_{xc} with a Hubbard correction as proposed by Anisimov et al. [44]. With an implementation proposed specifically for GGA by Dudarev et al [43] this will take the following form:

$$E^{GGA+U} = E^{GGA} + \frac{U}{2}\sum_{\sigma}[(\sum_{m} n_{m,m}^{\sigma}) - (\sum_{m,m'} n_{m,m'}^{\sigma} n_{m',m}^{\sigma})]. \tag{3.29}$$

U remains fixed as an approximation of the effective value U_{eff}. As in the definition of the Hubbard U term, n is the occupancy in a d orbital. The subscripts of n are the orbital momentum $m, m' = (-2, -1, 0, 1, 2)$ and electron spin $\sigma = (-1, 1)$.

In practice, the occupancy n is a matrix obtained by projecting the single electron wave function onto the d orbital states in the PAW method since the differing sites are within the augmentation region of the cores. The occupancy matrices are acquired using pseudo plane waves as a basis:

$$n_{m,m'}^{\sigma} = \sum_{n,\mathbf{k}} f_{n,\mathbf{k}}^{\sigma} \left\langle \tilde{\phi}_n^{\mathbf{k},\sigma} \middle| p_{m,m'} \middle| \tilde{\phi}_n^{\mathbf{k},\sigma} \right\rangle. \tag{3.30}$$

$p_{m,m'}$ is the projection operator and $f^{\sigma}_{n,\mathbf{k}}$:s are orbital occupancy numbers. Since n is computed using highly localised wave functions, we can assume that: $\sum_i |\tilde{\phi}_i\rangle \langle \tilde{p}_i| \approx 1$. Using this, the occupancy matrix can be rewritten in a simpler form using the occupancy of each augmentation channel ρ^{σ}_{ij}:

$$n^{\sigma}_{m,m'} = \sum_{(i,j)} \rho^{\sigma}_{ij} \left\langle \tilde{\phi}_{ni} \middle| \tilde{\phi}_{nj} \right\rangle .$$

3.10 Atomic forces

3.10.1 Hellmann – Feynmann theorem

The atomic forces acting on atoms can be derived using the Hellmann-Feynmann theorem. The method itself is not limited to atomic forces, but works for any Hermitian Hamiltonian $\hat{H}$ described with normalized wave functions ψ for any smoothly varying parameter P with an eigenvalue of E. The theorem can be proved by differentiating $E = \langle \psi | \hat{H} | \psi \rangle$ with the parameter P.

$$\begin{aligned}
\frac{\partial E}{\partial P} &= \left\langle \frac{\partial \psi}{\partial P} \middle| \hat{H}\psi \right\rangle + \left\langle \psi \middle| \frac{\partial \hat{H}}{\partial P}\psi \right\rangle + \left\langle \psi \middle| \hat{H}\frac{\partial \psi}{\partial P} \right\rangle \\
&= E\left(\left\langle \frac{\partial \psi}{\partial P} \middle| \psi \right\rangle + \left\langle \psi \middle| \frac{\partial \psi}{\partial P} \right\rangle \right) + \left\langle \psi \middle| \frac{\partial \hat{H}}{\partial P}\psi \right\rangle \\
&= \langle \psi | \frac{\partial \hat{H}}{\partial P} | \psi \rangle . \qquad (3.31)
\end{aligned}$$

The theorem results from $\hat{H}$ being Hermitian, meaning that $\langle \psi | \psi \rangle = 1$. This results in the part in the parentheses being equal to zero, completing the proof. We can use Hellmann-Feynmann theorem to calculate atomic forces under a potential by taking P to be a nuclear coordinate $\mathbf{R}_l$. The requirements for this are met under the Born-Oppenheimer approximation that was made earlier in the section [3.1]. Now taking the generalized force acting on a nucleus $\mathbf{F}_l$ by differentiating the total energy expressed by $E = \langle \psi | \hat{H} | \psi \rangle$:

$$\mathbf{F}_l = -\frac{d}{d\mathbf{R}_l} \langle \psi | \hat{H} | \psi \rangle ,$$

we can use the Hellmann-Feynmann theorem (3.31):

$$\mathbf{F}_l = -\langle \psi | \frac{\partial \hat{H}}{\partial \mathbf{R}_l} | \psi \rangle = -\frac{\partial E_0}{\partial \mathbf{R}_l}.$$

Now plugging in the energy functional (3.8) and differentiating with the nuclear coordinate $\mathbf{R}_l$, the universal functional vanishes, leaving only:

$$\mathbf{F}_l = -\int n \frac{\partial \hat{V}_{ext}(\mathbf{R}_l)}{\partial \mathbf{R}_l} d^3\mathbf{r}. \tag{3.32}$$

The atomic forces can therefore be derived using the external potential $\hat{V}_{ext}$ describing the electric potential of electrons interacting with the nuclei and electron density n.

3.10.2 Forces in PAW-mehod

As in the case of energies and wave functions in PAW, the forces imposed to the atomic cores are spread into three parts, with an additional part to correct the exchange correlation potential with interaction with pseudized core bound electron density $\tilde{n}_c$ from section [3.8.2]. The force is then:

$$\mathbf{F}_{PAW} = \mathbf{F}^1 + \mathbf{F}^2 + \mathbf{F}^3 + \mathbf{F}^{nuc}. \tag{3.33}$$

The first part $\mathbf{F}_l^1$ has a form similar to the force outside the augmentation region (3.32). In the case of PAW, however, its physical meaning is the force due to the change in the local potential $\tilde{v}_{eff}$ around the nuclei if the other ions are moved:

$$\mathbf{F}_l^1 = -\int [\tilde{n}(\mathbf{r}) + \hat{n}(\mathbf{r})] \frac{\partial v_H[\tilde{n}_{Zc}](\mathbf{r})}{\partial \mathbf{R}_l} d\mathbf{r}.$$

The second term $\mathbf{F}_l^2$ describes the force due to changes to the compensation charge due to $\hat{n}$:

$$\mathbf{F}_l^2 = -\sum \tilde{v}_{eff}(\mathbf{r}) \rho_{ij} q_{ij}^L \frac{\partial g_l(|\mathbf{r} - \mathbf{R}_l|) Y_L(\mathbf{r} - \mathbf{R})}{\partial \mathbf{R}_l} d\mathbf{r}$$

Together the first and the second terms describe the electrostatic contribution to the force acting on the nuclei. The changes in the compensation charge $\hat{n}$ that cause the second force term $\mathbf{F}_l^2$ are described with a function $\hat{D}_{ij}$. The other physical interpretation of this function is to take into account the difference of moments between the real and the pseudo wave functions. Its specific form is:

$$\hat{D}_{ij} = \sum_L \int \tilde{v}_{eff}(\mathbf{r}) Q_{ij}^L(\mathbf{r}) d\mathbf{r}.$$

The next contribution $\mathbf{F}_l^3$ is due to the change in the projector functions $\tilde{p}_i$ and it can be expressed using the potential strength parameters $\hat{D}_{ij}$, D_{ij}^1 and $\tilde{D}_{ij}^1$ that describe the change in the charge densities $\hat{n}$, n^1 and $\tilde{n}^1$ respectively. The third contribution to force is then:

$$\mathbf{F}_l^3 = -\sum_{n(i,j)} (\hat{D}_{ij} + D_{ij}^1 - \tilde{D}_{ij}^1 - \epsilon_n q_{ij}) \times f_n \left\langle \tilde{\phi}_{n\mathbf{k}} \right| \frac{\partial \left| \tilde{p}_i \right\rangle \left\langle \tilde{p}_i \right|}{\partial \mathbf{R}_l} \left| \tilde{\phi}_{n\mathbf{k}} \right\rangle,$$

where:

$$D^1_{ij} = \langle \varphi_i | - \frac{1}{2}\nabla^2 + v^1_{eff} \, | \varphi_j \rangle$$

and

$$\tilde{D}^1_{ij} = \langle \tilde{\varphi}_i | - \frac{1}{2}\nabla^2 + \tilde{v}^1_{eff} \, | \tilde{\varphi}_j \rangle + \sum_L \int_{\Omega_r} \tilde{v}^1_{eff}(\mathbf{r}) \hat{Q}^L_{ij}(\mathbf{r})).$$

D^1_{ij} and $\tilde{D}^1_{ij}$ are calculated on a radial grid within each augmentation region. The last contribution $\mathbf{F}^{nuc}$ is due to the interaction of non linear correction $\tilde{n}_c$ with the exchange correlation potential:

$$\mathbf{F}^{nuc} = - \int v_{xc}[\tilde{n} + \hat{n} + \tilde{n}_c] \frac{\partial \tilde{n}_c(\mathbf{r})}{\partial \mathbf{R}_l} d\mathbf{r}.$$

In the above, the effective one electron potential is $\tilde{v}_{eff}$. The changes in it changes cause the $\mathbf{F}^1_l$. Its form is:

$$\tilde{v}_{eff} = v_H[\tilde{n} + \hat{n} + \tilde{n}_{Zn}] + v_{xc}[\tilde{n} + \hat{n} + \tilde{n}_c],$$

whereas the other potentials used are:

$$v^1_{eff}[n^1] = v_H[n^1 + n_{Zc}] + v_{xc}[n^1 + n_c]$$

and

$$\tilde{v}^1_{eff}[\tilde{n}^1] = v_H[\tilde{n}^1 + \hat{n} + \tilde{n}_{Zc}] + v_{xc}[\tilde{n}^1 + \hat{n} + \tilde{n}_c].$$

4 Computational DFT

This section is dedicated to the computational details of the calculations performed, the convergence tests as well as a short explanations of the methods used in further analysis.

All calculations in this thesis were done with the plane wave pseudo potential code, Vienna Ab Initio Simulation package (VASP) [60]. The valence electron interactions with atomic cores were described by projector augmented wave method (PAW) according to section 3.8 and the exchange correlation functional of electron density was described with generalized gradient approximation (GGA) according to Perdew, Burke and Ernzerhof elaborated in section 3.6. The PAW potentials used in this study were the most recent ones available.

4.1 Unit cell

Hematite has a close packed crystal structure R3c (167) in Hermann Manguin notation. The conventional cell in this case is composed by 12 Fe and 18 O atoms. The initial structure of the conventional cell of hematite was taken from the materials-project website [51] and then ionic relaxations were performed until the forces were converged within the accuracy specified as per the Hellmann- Feynmann theorem. These forces are discussed more thoroughly in sections 3.10.1 and 3.10.2. In this iterative process of relaxation, each ionic step was done using the conjugate gradient algorithm [62]. The structure is allowed to relax according to these forces until the energy difference between iterations was $< 1 * 10^{-6}$eV. The relaxed structure is presented in figure 2.

The optimized lattice parameters were in agreement with experimental results with $|a| = |b| = 5.105$ and $|c| = 13.913$. For reference, the experimental results are $|a| = |b| = 5.028$ and $|c| = 13.824$ [64]. The slight overestimation of the lattice parameters is well reported when using the GGA+U method [37] and these results are a compromise between the lattice parameters and acceptable band gap further discussed in the coming section 4.2.3. Because hematite is a semiconductor, we use tetrahedron method with Blöch corrections for electron smearing [61]. To calculate the electronic structure, we use the Hubbard U correction 4.2.3. All calculations were spin polarized. The magnetic moments used were $5.0\mu_B$ for Fe and $0.6\mu_B$ for O and C.
All of the above holds for all the calculations in this thesis, unless stated otherwise.

4.2 Optimizing the computational model

In this section some special computational values are discussed. These values need to be converged separately for each different system and therefore many values need to be tested. These values were then used to arrive to the unit cell structure in figure 2.

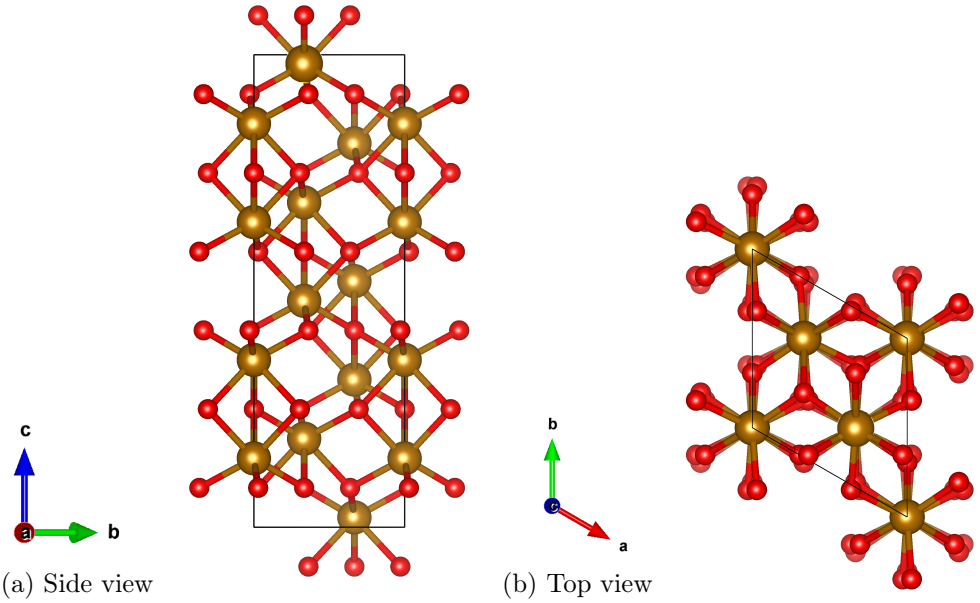

(a) Side view (b) Top view

Figure 2: A side and top view of the α-Fe_2O_3 unit cell. From the side view, one can take notice of the alternating layers of Fe and O. The top view demonstrates a hexagonal structure due to each iron adopting octahedral coordination chemistry; each iron bonding with six oxygen ligands. The angle between the lattice vectors a and b is 120 with c pointing perpendicularly to the plane

4.2.1 K-grid

The importance of the selection of special k-points was explained in the section 3.7. To quickly recap, these special points in the reciprocal space are chosen so that the single electron wave functions (3.20) can be summed from plane waves using finite points in the reciprocal space. These specially selected k-points are used as an approximation for the relevant values of the wave vector k, which bears the relevant single electron wave functions. With more of these k-points, the accuracy of the calculations will surely increase, but so does the computational burden. To get an accurate, yet computationally cheap selection of k-points, a convergence test was performed.

The method for generating a grid of selected special k-points in this study is the Monkhorst - Pack scheme [40] centered at the mid point of the Brillouin zone, known as the gamma (Γ) point. This scheme produces an evenly spaced grid of k-points but with different densities in each direction noted by $[\mathbf{k}_a, \mathbf{k}_b, \mathbf{k}_c]$. The results of the convergence test using grids of different densities is plotted in figure 3. The grid picked for this study according to the convergence study was $[5, 5, 2]$ corresponding to a k-grid of 50 points.

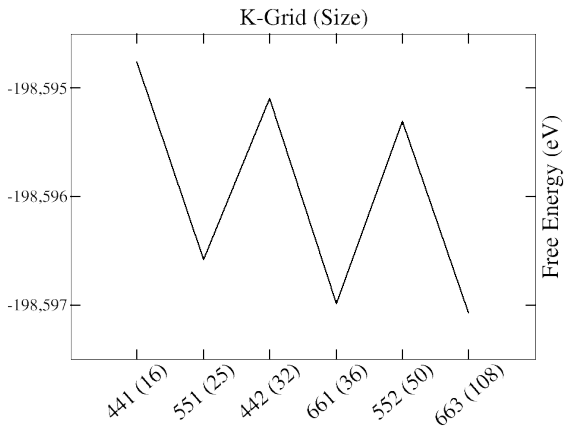

(a) K-grid convergence test

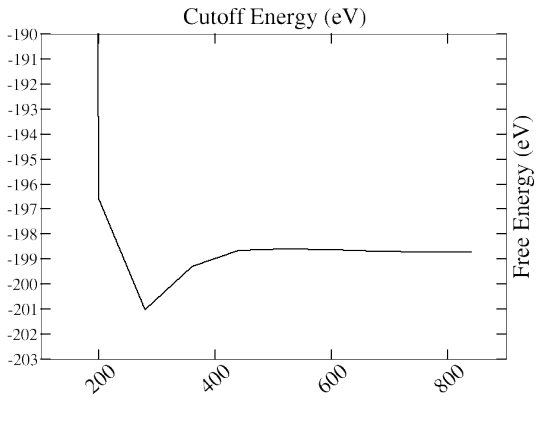

(b) Plane wave energy cutoff convergence test

Figure 3: The results of convergence tests performed on the density of the k-grid and the cutoff energy. The k-grid is given in the $[\mathbf{k}_a, \mathbf{k}_b, \mathbf{k}_c]$ notation and the overall size of the grid is presented inside the parentheses. The cutoff energy is given in electron volts. The total free energy of the structure is represented in the y-axis in both cases, each in different scale. The differing cutoff energy had a much greater impact on the total free energy of the system than a differing k-grid.

4.2.2 Plane wave cutoff energy

The second parameter requiring a convergence test is the plane wave kinetic energy cutoff, also elaborated in section 3.7. Its definition is given by equation (3.21). The physical meaning of the cutoff energy is the highest kinetic energy that the plane waves can have when they are used to describe electrons. Larger cutoff energies then allow for sharper features and higher accuracy, again with the immensely increased computational cost. As it is again a question of accuracy against practicality, a convergence test was performed. Its results are plotted in the figure 3 alongside the k-grid convergence picture. As convergence was reached with a value of 600eV, this value was picked for this study.

4.2.3 Hubbard U correction

Regular DFT calculations using LDA and GGA have been reported to severely underestimate band gaps and magnetic moments of the atoms in the case of transition metal oxides such as hematite. This implicates inability to accurately describe the electronic structure in the system. The reason for this error is failing to take into account that the electrons are transferred between significantly different environments such as in our case; from a transition metal to an oxygen.

To correct this mishap, we used isotropical Hubbard U correction with generalized gradient approximation [43]. The details of this method are further expanded upon in section 3.9 and its correction to the total energy is presented in equation (3.29).

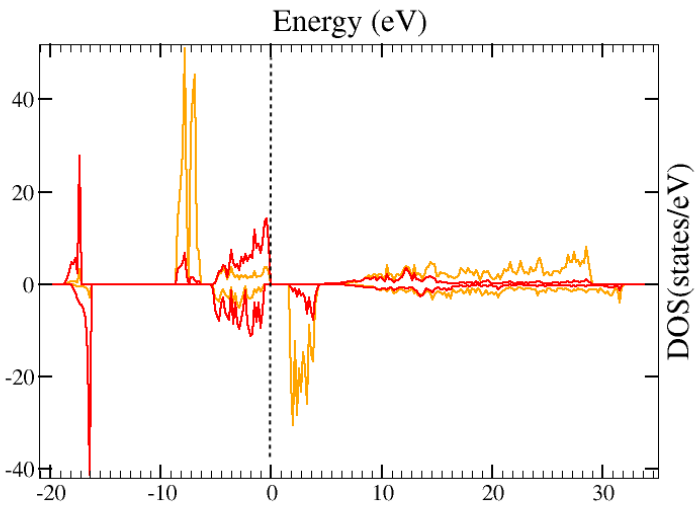

Figure 4: Density of states of the hematite cell. Orbitals of each atom type are not plotted separately, but as total density of states. The orbitals of iron are coloured with yellow and the orbitals of oxygen with red. Spin up is plotted on the positive side of the y-axis and spin down to the negative side. There are no orbitals on the Fermi level set at 0 eV on the x-axis, making hematite a semiconductor with a band gap of 2.0 eV.

A study by Meng et al. [37] compared different methods of DFT for transition metal oxides and in the case of α-hematite found that GGA with U correction yielded the accurate band gaps and magnetic momenta. The choice for the right value of U is heavily case dependent. Too large of a value will overestimate the cell size and too small of a value will underestimate the band gap. In the materials project website [39], U values were calibrated for different transition metal oxides using experimental binary formation enthalpies. The correction proposed here for Fe is U = 5.3 eV. Similar recommendation of U = 5 eV for a hematite (001) surface was also proposed by a DFT study by Rohrbach et al. [38]. Using the value U = 5.3 eV yields an acceptable band gap of 2.0 eV within the experimentally observed values between 1.9 eV to 2.2 eV. The density of states is presented in the figure 4.2.3. This value was therefore picked up for the Hubbard U correction term.

4.3 Surface slab

In first principles calculations, the most common model for the representation for a surface is that of the slab [63]. A surface cell then consists of two regions; a layer of the material in question and a vacuum on one direction. In this study, the slab was generated by expanding the bulk structure in figure 2 by duplicating it in the direction of the a and b vectors. This addition to width is done to prevent the adsorbing CO_2 from interacting

with itself as the cell is repeated due to periodicity in all directions in space. In the direction of the c vector then, sufficient vacuum region is added. As hematite has a hexagonal structure, the (001) surface can also be expressed using a Bravais-Miller index, which has four representing digits (0001). This is more often used in the literature for this kind of surface. The added vacuum region along the Z direction ensures that the periodicity is cut along this direction, while the lattice is repeated infinitely along X and Y directions.

The change from the bulk cell into a slab cell demands some changes. Firstly, as the reciprocal space scales inversely with the real space, the used k-point grid needs to be changed accordingly from [552] to [331]. Secondly the addition of the vacuum forces one to use only one k-point in the direction of c. This is done to prevent dispersion through the vacuum. The latter requirement forces to change the way that partial occupancies of orbitals are calculated. The formerly used tetrahedron method cannot be used as it requires subdividing the Brillouin zone into terahedrons, now not possible with only one k-point in the c direction. The smearing is then replaced with Gaussian smearing along with a small smearing width of 0.05eV.

In this study, the original thickness of the bulk structure was demonstrated to be sufficient when observing the relaxed slab structure. The relaxation of the slab structure occurred within the two outermost atomic layers leaving the bulk virtually unchanged. This is within the expectation as low energy electron diffraction data on metals and ionic compounds suggest the surface relaxations to occur within the three outermost layers [63].

4.3.1 Vacuum thickness

The thickness of the vacuum needs to be wide enough. As the program repeats the cell structure, the resulting layers of slab should not interact with each other. This problem can be solved with a convergence test. The results of the test are plotted in figure 6. The slight dip between values of 14.5Å and 17.0Å in the free energy implicates its convergence. This value was then chosen for this study. As the vacuum thickness increases after this point, its influence in free energy diminishes. Therefore, slab to slab interaction factors scaling with the thickness of the vacuum have lost their influence.

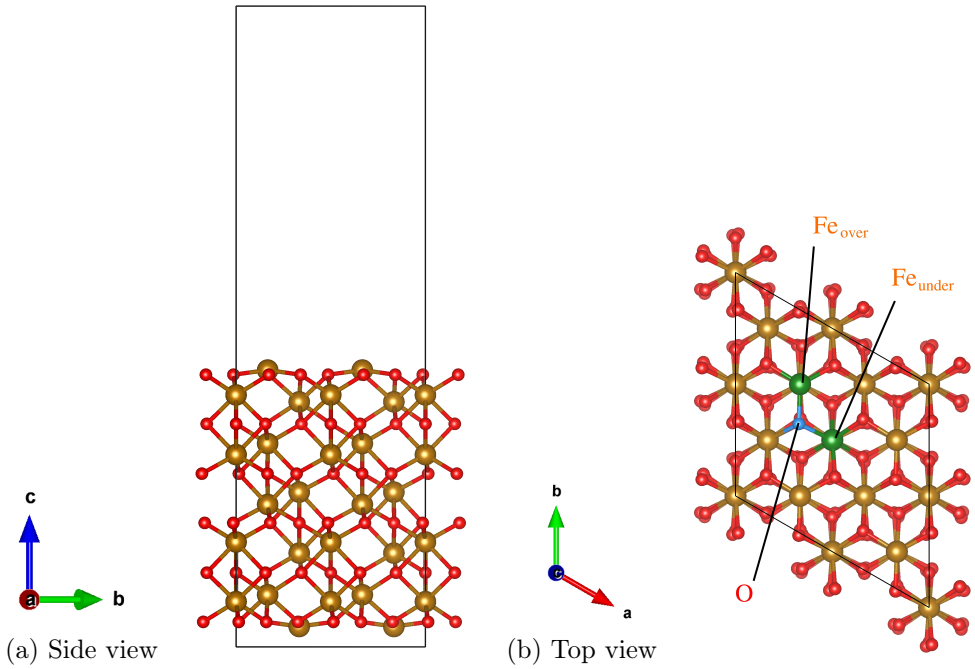

(a) Side view (b) Top view

Figure 5: A side- and a top view from the relaxed hematite slab. The relevant sites for doping and addition of CO_2 are marked in the top view with different coloring and labels. The relaxation of the slab has resulted in slight compression of the outermost Fe atoms into the slab.

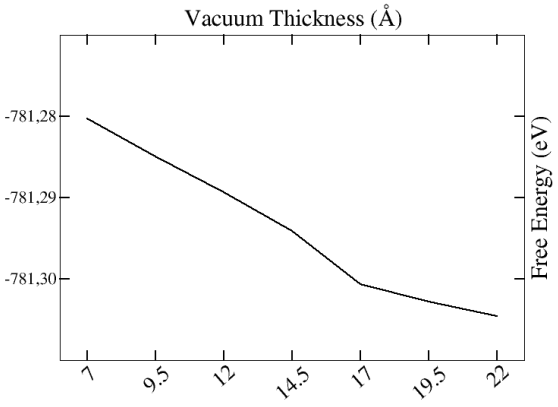

Figure 6: The convergence test of the thickness of the vacuum in the slab cell.

4.3.2 Relaxed slab structure

On the relaxed surface of the Fe_2O_3 slab there exists four different kinds of atoms along with three different bonds connecting oxygen and iron. We are considering the symmetrically non equivalent atomic sites for further analysis. Iron atoms on the surface were situated in three different depths: one at the outermost layer of the surface and two at inner layers. As the two inner layers have roughly the same surroundings, they are not considered separately from now on. Oxygen atoms were all located in the same depth, each forming three bonds to the differing iron atoms. The relaxed surface structure of hematite is plotted in figure 5. The relevant sites for doping and addition of CO_2 are on the outermost Fe from the slab, any of the O:s on the surface and finally one of the Fe:s lower than the outermost oxygen layer. From now on, these sites shall be referred to as: Fe_{over}, Fe_{under} and O. The subtext of the Fe:s refers to the ion being either over or under the outermost oxygen layer.

4.3.3 Adsorption of CO_2 on the Fe_2O_3 (0001) surface

Before attaching to the slab a separate system of just the CO_2 molecule was relaxed using the same computational values as with the rest of the calculations. The resulting structure was a straight CO_2 molecule, with bond lengths of 1.16Å. These lengths match perfectly with previous data on C=O bonds and is therefore an accurate model for the molecule.

CO_2 was added on the surface in eight different configurations atop each atom of interest (Fe_{over}, Fe_{under} and O) in either vertical or horizontal configuration for Fe's and on horizontal configuration for O, on bonds between the O and the Fe:s horizontally and finally a separate location was selected on a hollow site atop an oxygen in the inner layer as a vertical addition. The positions are shown in figure 7. The distances used between the site and the contacting atom in CO_2 varied and are rough estimations of the real distance in each case. The used values are Fe-O = 1.8Å, Fe-C = 2.2Å, O-O = 1.2Å and O-C = 1.4. This thorough investigation by using so many different configurations is necessary, because not a lot of information is available about CO_2 adsorption as of writing this thesis. The configurations might also reveal additional trends that might be relevant for future implementations.

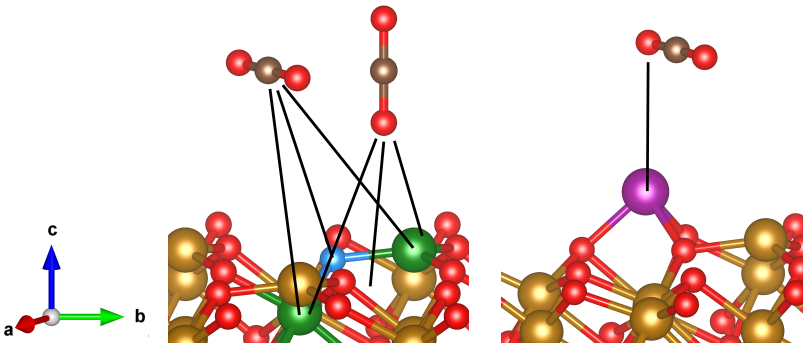

Figure 7: The initial positions of CO_2 on the slab. For the pristine and substitution defects with dopants three horizontal and vertical attachments are tried. One horizontal attachment was made for the interstitial dopant. The green and blue highlighted atoms in the left figure are the Fe_{over}, Fe_{under} and O positions. In the right picture Mn atom is used as an example coloured with purple.

4.4 Doping with Mn & Co

4.4.1 Choosing dopants

Manganese (Mn) was chosen for its performance in aiding in the Fischer–Tropsch synthesis; a reaction of reducing CO in the presence of hydrogen into hydrocarbons. The addition of MnO_2 nano sheets on hematite has been reported to significantly increase CO absorption and conversion [30]. This result was also verified earlier using MnO_2 coated Fe_2O_3 spindles [31]. The activation of CO might also translate to CO_2 and indeed, Mn has been favourable for CO_2 dissociation in similar materials due to the electron donation [16]. When considering the impact of Mn dopants on photocatalytic performance, a slight reduction of band gap has been observed [8]. This might indicate increased activity as the reduction of band gap in hematite increases the photoactivity under natural light, where the ideal for maximum absorption is between 1.3eV and 1.6eV [7].

Cobalt (Co) was chosen, since it has demonstrated potentially advantageous effects for catalytic activity as a hematite dopant. Co has been reported to increase the photocurrent in hematite nanorod arrays under a light source [1], demonstrating Co doping to be favourable for photocatalytic properties. This is supported also for Co doped bulk hematite by a dye degradation study [29]. Co has been shown to easily incorporate into the crystal lattice of hematite and reduce band gap and charge carrier recombination [28], allowing for more excitations by light and longer lifetime for them, overall increasing the chance for a catalytic reaction. Finally Co dopant lowers the oxygen evolution reaction overpotential of hematite [8] which is an anode reaction for the cathodic reduction of CO_2 in electrocatalysis.

We will be doing a comparative study by employing both Co and Mn. Both are transition metals with either one more or less electron occupying the d-orbital than Fe. It will be possible to observe the trends to ascertain if materials with lower or higher number of d-electrons should be used for possible photo catalytic experiments.

4.4.2 Doping the hematite slab

The site of interest for doping is the site of the atoms outlined by the CO_2 attachments in section 4.3.3. In total, five different ways of doping were used. Substituting dopants were inserted at the hematite slab at two different positions, those being Fe_{over} and Fe_{under}. Also, interstitial dopants were placed on Fe_{over}, Fe_{under} and O. Since Mn and Co are transition metals, it's likely that they occupy the same positions as Fe and therefore substituting them with the O position is unlikely to produce relevant results.

The effect of doping on CO_2 activation will be thoroughly investigated using the same CO_2 positions as in figure 7, keeping the initial distances same in the case of substituting dopants, while different CO_2 initial positions will be used in the case of interstitial dopants. By using the same initial positions of CO_2 with the substituting dopants, the possible effects of doping are expected to be clearly demonstrated. However, only the CO_2 initial positions in the vicinity of the dopant are investigated. In the case of interstitial dopants, it is harder to draw such comparison because of the differing surface structure due to the interstitial atom. Therefore, for each relaxed interstitial dopant, one horizontal CO_2 initial position was used.

The Hubbard U corrections and magnetic moments for the dopants are acquired from the materials project [39]. The same methodology for determining the dopant U values is used as in the case of Fe for consistency. The values are: U_{Mn} =3.9eV and U_{Co} =3.3eV. Magnetic moments are $\tau_{Mn} = 5.0\mu_B$ and $\tau_{Co} = 0.6\mu_B$.

4.5 Bader charge analysis

As the electrons in the system are represented by a continuous electron density, the question of which electron belongs to which core leaves some ground for debate. Also, the atomic charges are not observables in quantum theory, and are not intrinsically defined. *Atoms* themselves therefore lack a definition. The entirety of classical chemistry of atoms and their bonds is then under some scrutiny.

However, the basic theories offer a good insight and definitions of different reactions. As the classical definitions might not be specific, they offer tools for understanding the results found in the world of quantum chemistry. In this thesis, the definition by Bader [47] is used to distinguish atoms. The algorithm for computing if from data is made by Henkelman et al. [48]. Bader charge analysis is based on charge density and its definition of an atom is straightforward and practical. Taking gradient of the electron density ∇n yields a vector field in which every coordinate has a direction pointing to the maximum increase of n. An atom can be defined in this field by finding zero-flux surfaces $S(\mathbf{r}_s)$ where each point $\mathbf{r}_s$ satisfies:

$$\nabla n(\mathbf{r}_s) \cdot \mathbf{v}(\mathbf{r}_s) = 0, \tag{4.1}$$

where $\mathbf{v}(\mathbf{r}_s)$ is a unit vector normal to the surface $S(\mathbf{r}_s)$. In this two dimensional surface, the electron density reaches a local minimum, this typically occurs somewhere in between the cores. These local minima expose clear regions of space around the cores known as

Bader volumes. The charge inside can be taken as a good approximation of the atomic charge and the zero flux surface to enclose atoms.

The algorithm by Henkelman et al. evaluates the gradient of the density ∇n in each given grid point. A line is drawn from the starting grid point to another point in the direction of the largest addition of density n, eventually leading to an atomic core. The zero flux surfaces $S(\mathbf{r}_s)$ are not defined explicitly, but the dividing of space into atoms is done by categorizing each path drawn path by their final destinations: the atomic cores. The computational burden scales up with more grid points.

5 Results and Discussion

In this section, the various results of the calculations are presented followed by a discussion on the findings collected on a single section 5.2. The section then concludes on additional results based on this reflection.

5.1 CO_2 absorption on Fe_2O_3

For CO_2 reduction, splitting of the molecule when relaxing it upon the surface is the best outcome, but not essential for useful material for this purpose. For a surface to be catalytically active, the reactant species should be thermodynamically stable on the catalytic surface [24]. This means that after the atomic relaxation of the structure, CO_2 should at least remain bonded to the slab.

Specifically CO_2 reduction reactions on a catalyst tend to follow a similar pattern. The notorious inactivity of the CO_2 molecule is due to its high bond energy of 750 kJ mol^{-1} as well as its geometry. In some catalysts, CO_2 can bind to a surface in a bent configuration, in which the molecule exhibits lower LUMO level and therefore is more susceptible to receiving an electron [23]. This in turn might induce splitting. The received electron can come about in either an electrocatalytic or photocatalytic reaction leading to CO_2 reduction for an example. Too strong binding on the surface, on the other hand, might lead to catalyst poisoning, therefore weak binding is ideal for a catalyst material [17]. This means that after the adsorption, the surface itself should remain irreversibly unaltered.

In this study the CO_2 behaved on the surface in a variety of ways. Both Fe and O were active reaction sites and there was a clear attraction in between O of hematite with C in CO_2 and Fe with O in CO_2. This much has been reported earlier in similar theoretical studies [24] [59]. Relaxing CO_2 onto the undoped hematite did not result in CO_2 splitting. The six initial CO_2 configurations resulted in chemisorption, weaker physisorption and separation from the slab in equal measures. The distances, bond lengths and angles are collected in table 1 and the resulted geometries are plotted in figure 8.

5.1.1 The effects of doping

As the initial six CO_2 configurations were relaxed upon the doped slab, the resulted geometries were almost identical to the ones without the doping. No splitting was present. Chemisorption, physisorption and inactivity occurred as with the undoped slab resulting in very similar structures. Therefore, in figure 8 they are not plotted separately. In the case of interstitial dopants, only physisorption occurred. The final configurations are plotted in the figure 9.

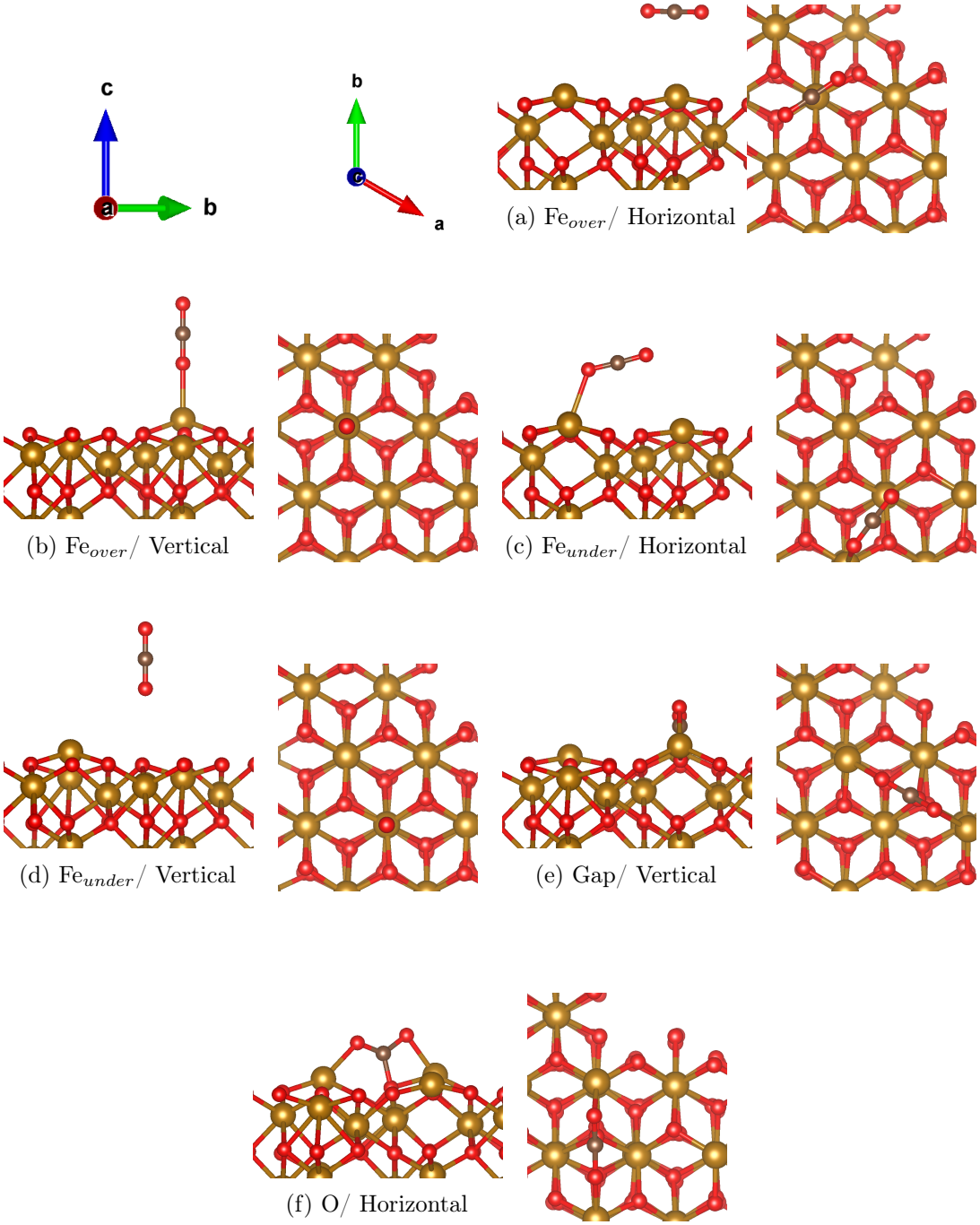

(a) Fe_{over}/ Horizontal

(b) Fe_{over}/ Vertical

(c) Fe_{under}/ Horizontal

(d) Fe_{under}/ Vertical

(e) Gap/ Vertical

(f) O/ Horizontal

Figure 8: Relaxed CO_2 on undoped hematite slab. These structures are named after the initial CO_2 position before relaxation for consistency. Chemisorption is present in (e) and (f) while physisorption occurred in (b) and (c). In (a) and (d), no adsorption occurred and CO_2 migrated away from the slab. The structure of CO_2 was altered during chemisorption and there is a notable bending and stretching of C-O bonds.

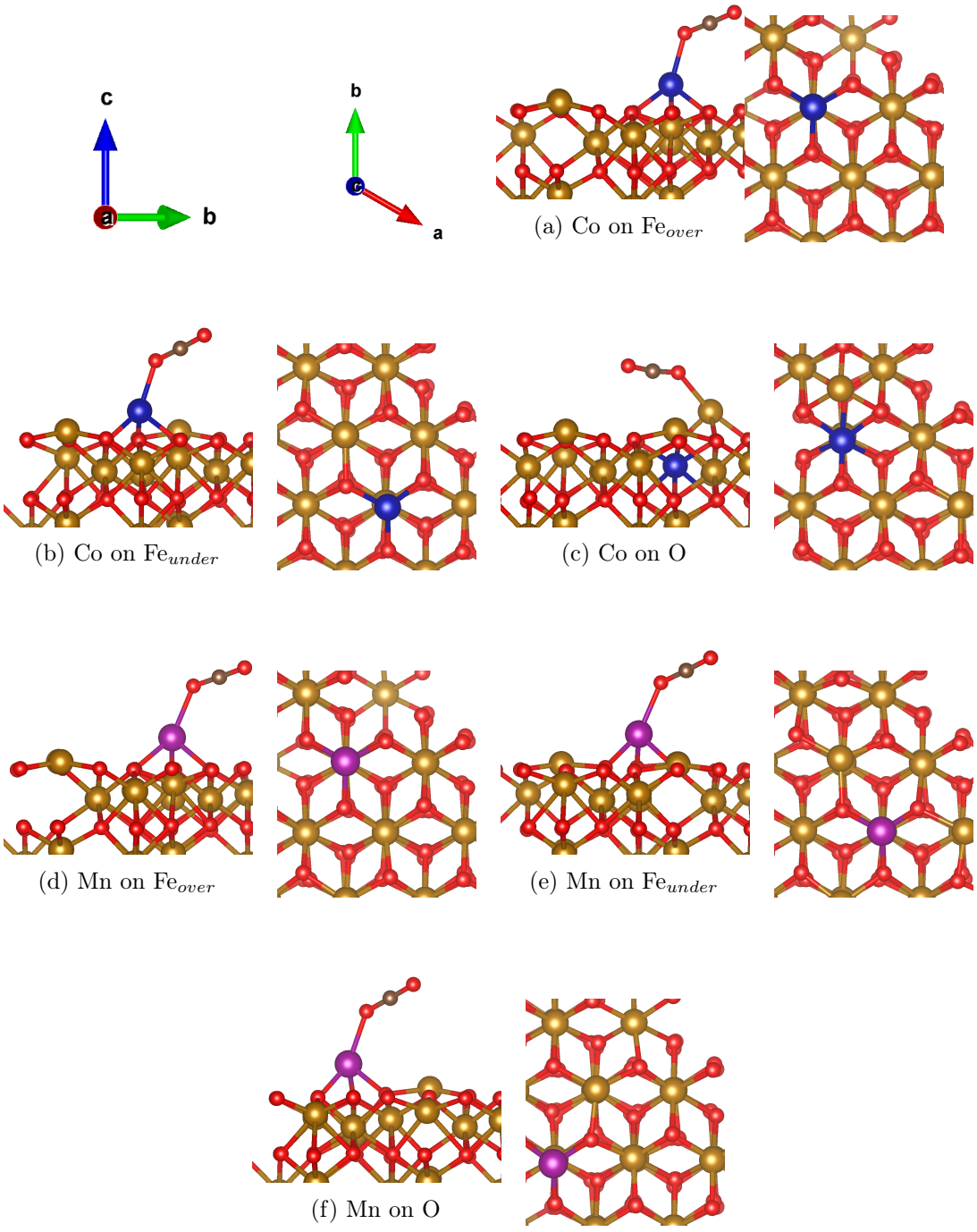

(a) Co on Fe_{over}

(b) Co on Fe_{under}

(c) Co on O

(d) Mn on Fe_{over}

(e) Mn on Fe_{under}

(f) Mn on O

Figure 9: The relaxed CO_2 positions on interstitial dopants from the side view and the final dopant migration sites from the top view. Only physisorption was present, but in all cases this did indeed occur. Interstitial dopants had remarkable effects on their surroundings, but still kept the hexagonal structure in the slab. The biggest difference between Co and Mn occurred when they were placed on the oxygen atom as Co then occupied an Fe_{under} position while Mn migrated to Fe_{over} position.

Configuration (Site/CO_2)	**CO_2 distance (Å)**	**CO_2 bond lengths (Å)**	**CO_2 angle (°)**
Fe_{over}/ Horizontal	No bonding		180
Fe_{over}/ Vertical	2.20 (Fe_{over} & O)	1.18 & 1.17	180
Fe_{under}/ Horizontal	2.29 (Fe_{over} & O)	1.19 & 1.17	180
Fe_{under}/ Vertical	No bonding		180
Gap/ Vertical	1.39 (O & C)	1.29 & 1.25	126
O/ Horizontal	1.38 (O & C)	1.26 & 1.29	127
Co_{over}/ Horizontal	No bonding		180
Co_{over}/ Vertical	2.19 (Co_{over} & O)	1.18 & 1.17	180
Co_{over}, Gap/ Vertical	1.36 (O & C)	1.29 & 1.26	126
Co_{over}, O/ Horizontal	1.37 (O & C)	1.26 & 1.30	127
Co_{under}/ Horizontal	2.29 (Fe_{over} & O)	1.19 & 1.17	180
Co_{under}/ Vertical	No bonding		180
Co_{under}, Gap/ Vertical	1.37 (O & C)	1.30 & 1.26	126
Co_{under}, O/ Horizontal	1.40 (O & C)	1.25 & 1.29	126
Mn_{over}/ Horizontal	No bonding		180
Mn_{over}/ Vertical	2.40 (Mn_{over} & O)	1.18 & 1.17	180
Mn_{over}, Gap/ Vertical	1.37 (O & C)	1.29 & 1.26	126
Mn_{over}, O/ Horizontal	1.39 (O & C)	1.25 & 1.29	127
Mn_{under}/ Horizontal	2.29 (Fe_{over} & O)	1.18 & 1.17	180
Mn_{under}/ Vertical	No bonding		180
Mn_{under}, Gap/ Vertical	1.40 (O & C)	1.29 & 1.25	127
Mn_{under}, O/ Horizontal	1.40 (O & C)	1.25 & 1.28	127
Int.Co_{over}/ Horizontal	2.13 (Int.Co & O)	1.19& 1.17	180
Int.Co_{under}/ Horizontal	2.12 (Int.Co & O)	1.19 & 1.16	180
Int.Co_O/ Horizontal	2.17 (Fe_{over} & O)	1.19 & 1.16	173
Int.Mn_{over}/ Horizontal	2.25 (Int.Mn & O)	1.19 & 1.17	180
Int.Mn_{under}/ Horizontal	2.25 (Int.Mn & O)	1.19 & 1.16	180
Int.Mn_O/ Horizontal	2.24 (Int.Mn & O)	1.19 & 1.16	180

Table 1: Structural overview of the relaxed CO_2 configurations. The CO_2 distance column reports the smallest distance between CO_2 and the slab and the neighbouring atoms. The bond lengths are given in the order where the bond closer to the slab comes first or where the bond is more parallel with the a lattice vector in the case of the chemisorbed structures.

5.1.2 Adsorption energies

Adsorption energy was used to measure the stability of CO_2 binding to the surface. Its definition is the energy difference between the full system and its constituents: the adsorbent and the adsorbate. In this case the adsorbent was the hematite slab and the adsorbate was the CO_2 molecule. Adsorption energy is expressed as:

$$E_{Ads} = E_{Sys} - [E_{Slab} + E_{CO2}]. \tag{5.1}$$

A larger negative E_{Ads} indicates more stability as well as exothermic adsorption of the CO_2 onto the slab [32]. It also hints to a stronger interaction between the two [33]. Both of these result in the adsorption being more likely in nature. The adsorption energies of CO_2 into different slab structures are collected in the table 2.

Doped or otherwise, generally the hematite slab was keen on adsorbing CO_2 with just one exception. An adsorption energy was more favourable with more activation from the CO_2. This is because the chemisorbed energies were more negative, than the energies of the physisorbed CO_2 configurations. Even as seems to be the trend, the most favourable adsorption was with the Mn on O interstitial dopant structure (figure 4.3.3 (f)). This indicates a very favourable adsorption and a tight bond that forms between Mn and O. This was generally the case for the other interstitial Mn configurations as well.

5.2 CO_2 binding discussion

This section is dedicated to discussing the most notable results so far and to guide the rest of the thesis to their direction. Analysis of all the numerous CO_2 and dopant configurations would hardly be relevant.

We see that there is significant chemisorption occurring on the surface. The chemisorbed CO_2 structure resulting from the relaxation of Gap/Vertical and O/Horizontal initial positions (see figure 8 for the structures) in doped and undoped slabs confirms earlier results for hematite [24] and is a strong indicator that hematite might be a suitable material for CO_2 reduction applications [23]. This sort of activation has been reported to precede splitting in similar materials in computational studies [25] [55] [56]. The bending of this magnitude of the C=O bonds has also been linked to their weakening in CO_2 using vibrational analysis [59], allowing them to be severed more easily. The chemisorbed structures are plotted in figure 8 labeled by (e) and (f). The structures are identical with the oxygens of CO_2 bonding with different Fe_{over} sites allowing carbon to possibly be attracted to the slab oxygens in between, causing the molecule to bend. As the O/Horizontal structure has good consistency with adsorption energies using dopants and the CO_2 is bonded to a Fe_{over} doping site this configuration is taken into further consideration. The aim of this is to uncover the specific effects that the dopants have in contact with CO_2 and the main mechanism behind the chemisorption. The O/Horizontal structure on doped and undoped slab will be investigated further using Bader charge analysis in the next section and the CO_2 will be reduced to CO to see the aftereffects of possible splitting.

Configuration (Site/CO_2)	**Adsorption energy (eV)**
Fe_{over}/ Vertical	-0.525
Fe_{under}/ Horizontal	-0.708
Gap/ Vertical	-1.353
O/ Horizontal	-1.494
Co_{over}/ Vertical	-0.219
Co_{over}, Gap/ Vertical	0.014
Co_{over}, O/ Horizontal	-0.512
Co_{under}/ Horizontal	-0.318
Co_{under}, Gap/ Vertical	-0.676
Co_{under}, O/ Horizontal	-0.979
Mn_{over}/ Vertical	-0.387
Mn_{over}, Gap/ Vertical	-0.206
Mn_{over}, O/ Horizontal	-1.422
Mn_{under}/ Horizontal	-0.687
Mn_{under}, Gap/ Vertical	-1.775
Mn_{under}, O/ Horizontal	-0.520
Int.Co_{over}/ Horizontal	-0.678
Int.Co_{under}/ Horizontal	-0.494
Int.Co_O/ Horizontal	-0.059
Int.Mn_{over}/ Horizontal	-1.462
Int.Mn_{under}/ Horizontal	-2.092
Int.Mn_O/ Horizontal	-2.441

Table 2: Adsorption energies of different configurations in which CO_2 stuck to the surface. The chemisorped structures are written with red and physisorped with blue.

Some results of doping are also quite clear at this stage. Doping the surface with Co showed that it has a generally unfavourable effect on CO_2 adsorption according to adsorption energies. These effects were less notable, when Co was not in a more bound site on the surface occupying the Fe_{under} position. The interstitial doping revealed that indeed; Co heavily prefers to occupy this position and when relaxing the initial structure of Int. Co_O in figure 9 (c), Co migrated to this position by pushing the original Fe outwards to the surface.

Mn on the other hand preferred a more outward position in the surface and always imitated the Fe_{over} configuration when using it as an interstitial dopant. The interstitial dopants were extremely attracted to the oxygen of CO_2 yielding very negative adsorption energies. The adsorption energies for the chemisorption of CO_2, Mn had mixed results while generally being a slightly negating factor. Still, Mn might be an excellent dopant for increasing active sites for CO_2 binding because it sticks to the surface and attracts CO_2 quite substantially. This might lead to an increased rate of chemisorption in a future application. This also might be a subtle invitation to use transition metals with more electrons in the d-orbital than Fe has.

5.3 Charge density difference

In this section, the charge density difference resulting from the chemisorption of CO_2 is investigated by visualising. The charge density difference Δn is calculated between the charge densities of the adsorbate A and the adsorbent B by simply subtracting the two from the charge density of the total system:

$$\Delta n = n_{AB} - n_A - n_B \tag{5.2}$$

In this study n_A is the charge density of CO_2 and n_B the density of the hematite surface without CO_2. The structure under investigation is the O/Horizontal structure ((f) in figure 8) with both cases of doping also investigated.

The change in charge density when the CO_2 adsorbs into the surface can tell many things about the adsorption mechanisms; which atoms have lost charge? Which orbitals were actively changing shape or losing/gaining electrons?
In figure 10 the charge density difference of pure hematite slab and free CO_2 (A & B) with the full system (AB) are plotted using the VESTA [49] software. In all the cases, the increase in electron density is concentrated on the oxygen atoms in the CO_2 molecule. The increase occurs above and below the atoms resembling a shape of a p-orbital. A decrease in charge density occurs mainly in the vicinity of the carbon atom and around the slab's bonding oxygen atom. Directly on the bond between the carbon and oxygen atom, there is also increase in charge density, indicating that the oxygen is bonding with the carbon.

Differences brought by the dopants follow a pattern corresponding to the increase of electrons on the 3d orbitals. Manganese has five 3d electrons, iron has six and cobalt has eight. The oxygen atom in CO_2 bonding to manganese experiences the most notable positive change in its charge density difference. A smaller change can be observed in the undoped case and least notable change in cobalt doped slab.

Manganese also occupies a slightly elevated position in the slab compared to the other two slab variations, providing another explanation for the varying density differences. The bond length remains roughly the same in each case. All charge density differences were localised in the immediate vicinity of the adsorbed CO_2 molecule in each case as is to be expected.

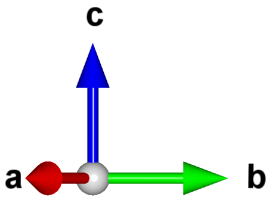

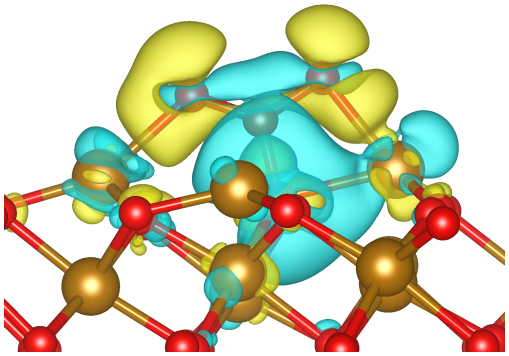

(a) Pure hematite slab

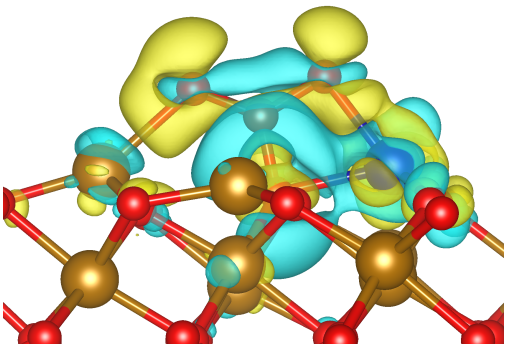

(b) Cobalt-doped slab

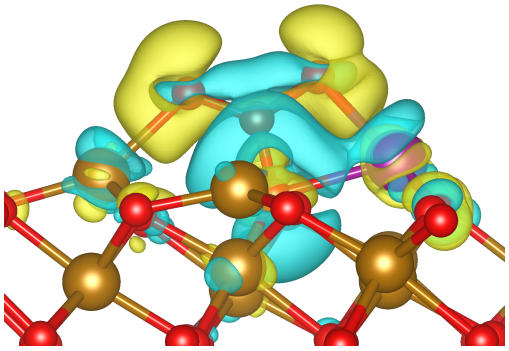

(c) Manganese-doped slab

Figure 10: Charge density difference of CO_2 adsorption to hematite slab. Yellow colour indicates an increase of electron density positive and blue a decrease. The doping site is the rightmost CO_2 bonded atom in the slab.

5.4 Bader charge analysis

Bader charge analysis introduced in the section 4.5 is used in this section to unveil the possible electronic attraction mechanisms behind the adsorption of CO_2 into hematite and quantify the results of the charge density difference in the last section.

This thesis uses the software by the Henkelman group [50] to calculate the net Bader population of each atom from VASP output files. From Bader population, the net Bader charge can be simply calculated by subtracting the charge of the frozen core electrons and Bader population from the atomic number:

$$z_{Bn} = z_{atom} - z_{frozen} - z_{Bp}. \tag{5.3}$$

This can be used as a good approximation for the atomic charge. The Bader net charges of each atom bonding to CO_2 are plotted on the figure 11. Here it is easy to observe electronic attraction that led to the chemisorption in this manner. This explains the tendency of iron atoms to attract the oxygen in CO_2 and the oxygen of the slab with carbon already noted as a trend in section 5.2. Iron seems to hold the largest positive charge despite the extra d electron of manganese. This implies that it stays localised around its original core. Cobalt also seems to remain unchanged with its lack of one valence electron compared to iron.

The adsorption of CO_2 causes changes to the charge density as was seen in figure 10. By calculating the net Bader charges of CO_2 and the hematite slab as separate systems, we can quantify the charge transfer between the atoms during the adsorption. This is done by simply subtracting the initial separate system net Bader populations from the atom's final populations in the adsorbed case.

The resulting changes in net Bader charges are plotted in figure 12 along with charge density differences. The most active site for charge transfer seems to be the doping site in the case of undoped and manganese doped case. Cobalt on the other hand transfers less charge compared to the iron site. The combined charge transfer of CO_2 was negative in all the cases, meaning a slight gain of electron affinity in CO_2:s part. The biggest transfer was with the undoped slab with a transfer of -0.17, slightly lower result with manganese doped slab with -0.16 and by far the least with cobalt doped with -0.09. This means that in all of the cases, no ionization is happening during the CO_2 adsorption.

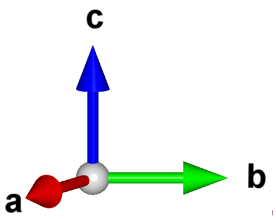

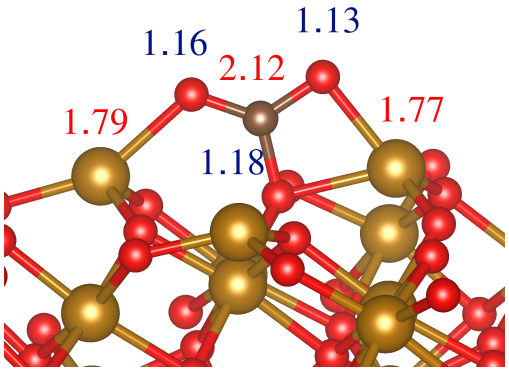

(a) Pure hematite slab

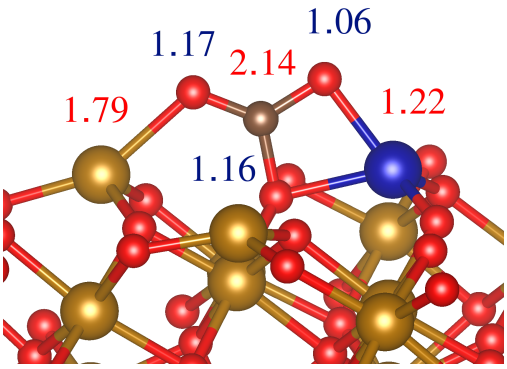

(b) Cobalt-doped slab

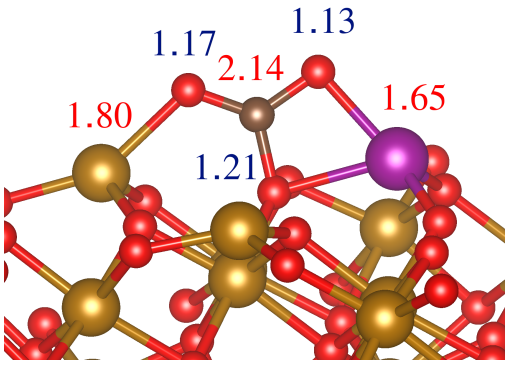

(c) Manganese-doped slab

Figure 11: The net Bader charge for each bonding atom in CO_2 adsorption. Red colour indicates positive net charge and blue negative net charge, both are expressed as a multiplier of a charge of one electron.

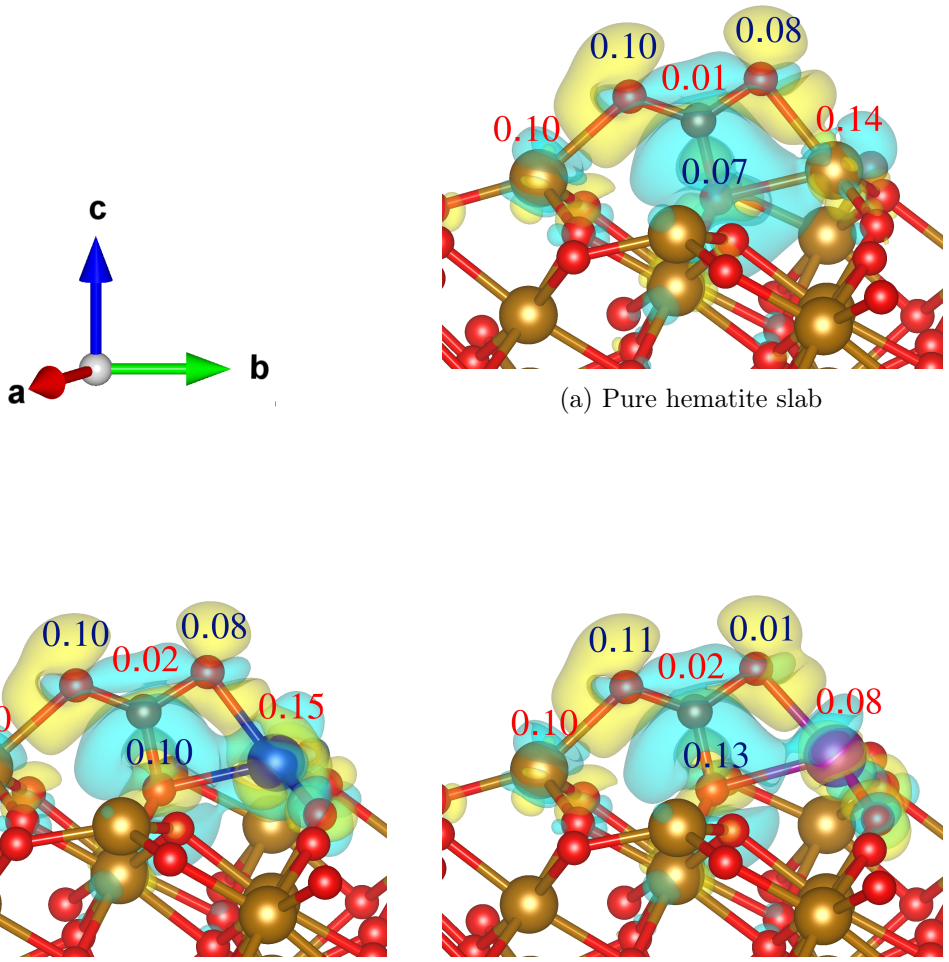

(a) Pure hematite slab

(b) Cobalt-doped slab

(c) Manganese-doped slab

Figure 12: The change of Bader charge in the bonding atoms due to CO_2 adsorption on the hematite slab. Red colour indicates positive change and blue negative change. The change is calculated as multiplier of charge of one electron, a negative change then means a relative gain of electron affinity.

5.5 CO_2 splitting

In this section an oxygen atom was removed from the chemisorped O/Horizontal and the resulting CO molecule was allowed to relax on the slab. The removal of either oxygens was investigated separately, meaning a removal of either the atom bound to the Fe_{over} doping site and the other bound to a different Fe_{over} atom. The reason for this is to investigate the possible aftereffects of the splitting of CO_2 molecule from the chemisorped configuration. Possible end positions might indicate different possibilities for further converting CO to different products such as hydrocarbons. The results of the relaxation with doped and undoped slab is plotted in figure 13.

In the case of a pristine hematite slab ((a)&(b) in figure 13), the CO molecule relaxed only slightly, leaving the molecule intact. The bond length between carbon and the oxygen in the slab slightly stretched for 0.01Å for (a) and 0.04Å for (b) structures. The slab remained virtually unchanged, implying that there is no catalyst poisoning while implementing this material for CO_2 splitting applications. All in all, this is a very favourable result and encourages more research on hematite.

In the case of a Co doped structure, the story is completely different. Removing either oxygen atom from CO_2 ((c)&(d) in figure 13) resulted in a formation of a new CO_2 molecule. The oxygen in the slab was more attracted to the carbon atom in CO than to the slab itself, leading to its dissociation from the slab. The formed CO_2 had either bent or straight geometry with shortened bond lengths in either case. If the addition of Co makes the surface of hematite volatile of losing oxygens, it is not a suitable dopant. The only positive factor might be the newly formed site on the slab with the oxygen vacancy defect, but the results from Bader charge analysis call this into immediate scrutiny. After the loss of oxygen, there is nothing to attract the carbon in CO_2 to bend the molecule if the atom is bonded to Fe_{over} at the site.

Mn as a dopant had mixed results completely depending on the removed oxygen of CO_2. In the case where the Mn bound oxygen was removed ((e) in figure 13) the results are resoundingly similar to earlier Co bound oxygen removal. This resulted in a bent, slab bound CO_2 structure dangling loosely on she slab. This was not the case when removing the Fe bound oxygen (f in figure 13). In that case, the resulting structure was unique to the ones reported before. There was no clear formation of CO_2, but the length of the bond between carbon and the slab bound oxygen was remarkably shortened by 0.12Å in the expense of the oxygen slightly migrating away from the rest of the slab. The results might be mixed, but they are in both cases negative for the splitting of CO_2, implying that the use of dopants for improving the properties of Fe_2O_3 might cause unwanted challenges of catalyst poisoning and decay.

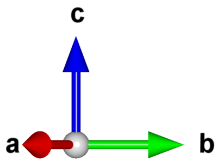

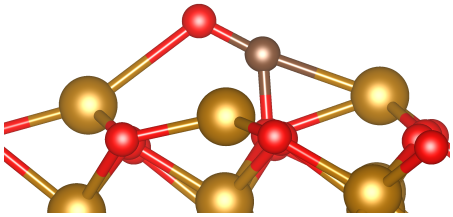

(a) Pristine, dopant side O removed

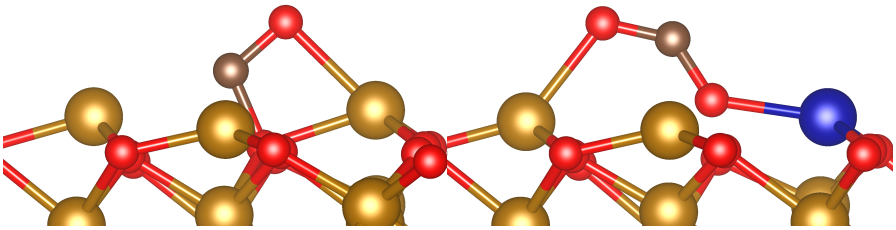

(b) Pristine, undoped side O removed (c) Co-doped, doped side O removed

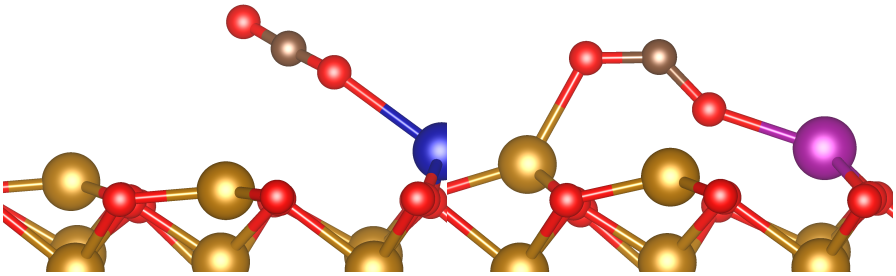

(d) Co-doped, undoped side O removed (e) Mn-doped, doped side O removed

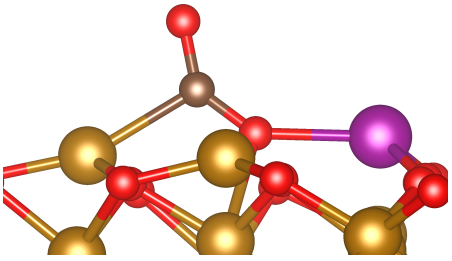

(f) Mn-doped, undoped side O removed

Figure 13: Results of removing an oxygen from chemisorbed CO_2.

6 Conclusions

This study conducted a literature review, followed by an investigation of CO_2 on doped and undoped α-Fe_2O_3 (0001) surface slab. Afterwards a Bader charge analysis was made on a chemisorbed structure of CO_2 followed by an additional study on the aftereffects of splitting the molecule into CO.

The space between the outermost Fe atoms acted as a reaction site bending the molecule to chemically more active chemisorbed 127° configuration. This means a significant weakening of C=O bonds [59] and lower LUMO level [23] according to the literature and a received charge affinity confirmed by Bader charge analysis. This result shows promise in possible future applications of hematite in this field of study. Doping had no notable effects on the structural chemisorption or physisorption of CO_2 but had a notable effect to adsorption energies, especially with interstitial Mn dopants forming strong bonds with O atoms of CO_2. Results of this thesis suggest that transition metals with more electrons than iron in their d-orbital might be better candidates for doping than those with less.

The dopants used in this study also had unfavourable effects. Their addition insertion made surrounding O atoms volatile, and addition of CO led to their dissociation from the surface forming new molecules of CO_2 in some cases. The interaction between CO and hematite is well reported and is the one of the carbothermic reactions (reducing metal oxides with carbon in high temperatures) used blast ovens in the process of reducing hematite ore into iron. This reaction did not occur in the undoped surface, but might limit the future methods used to harness the promising properties of hematite for the purpose of reducing CO_2.

7 Appendix

7.1 Slater determinant

In this section, the wavefunction of the Kohn-Sham system is discussed. In practical DFT calculations there is no need for the all electron Kohn-Sham wavefunction to be formed from single particle solutions to the Kohn-Sham equation (3.10), but this theoretical discussion is given to explain the basic properties of it for added clarity.

In the Kohn-Sham method, the electrons are described as noninteracting fermions. This means that the Kohn-Sham system is antisymmetric with respect to exchanging particles within it. When exchanging two particles then, the sign of the all electron wave function of the system changes signs: $\Phi(a, b, c..) = -\Phi(a, c, b...)$. A mathematical entity for conserving this antisymmetric property when constructing the all electron wave function from single particle solutions is known as a Slater determinant. In the case of two particles the Slater determinant takes a form:

$$\Phi_2(\mathbf{x}_1, \mathbf{x}_2) = \phi_1(\mathbf{x}_1)\phi_2(\mathbf{x}_2) - \phi_1(\mathbf{x}_2)\phi_1(\mathbf{x}_2).$$

Here $\mathbf{x}$ denotes position $\mathbf{r}$ as well as spin. In a general case of N particles we can construct a determinant with a normalizing factor:

$$\Phi_N(\mathbf{x}_1, \ldots, \mathbf{x}_N) = \frac{1}{\sqrt{N!}} \begin{bmatrix} \phi_1(\mathbf{x}_1) & \ldots & \phi_N(\mathbf{x}_1) \\ \vdots & \ddots & \vdots \\ \phi_1(\mathbf{x}_N) & \ldots & \phi_N(\mathbf{x}_N) \end{bmatrix}. \tag{7.1}$$

7.2 Reciprocal lattice

Let us first set an infinite array of points forming a Bravais lattice in three dimensions i.e. points that can be generated using a discrete translation operation R in each of its points.

$$\mathbf{R} = n_1\mathbf{a}_1 + n_2\mathbf{a}_2 + n_3\mathbf{a}_3. \tag{7.2}$$

Secondly let us define a plane wave with a wave vector $\mathbf{G}$ so that it has the same periodicity as our Bravais lattice:

$$e^{i\mathbf{G}(\mathbf{r}+\mathbf{R})} = e^{i\mathbf{G}\mathbf{r}}. \tag{7.3}$$

This relation shall hold for any $\mathbf{r}$ and $\mathbf{R}$ in the Bravais lattice. The set of all wave vectors $\mathbf{G}$ that satisfy this relation is known as the reciprocal lattice for the Bravais lattice set up by $\mathbf{R}$ [34]. The lattice set up in real space is known as the direct lattice.

The reciprocal lattice is also a Bravais lattice and can be generated from the direct lattice using its primitive vectors:

$$\mathbf{b}_1 = 2\pi \frac{\mathbf{a}_2 \times \mathbf{a}_3}{\mathbf{a}_1 * (\mathbf{a}_2 \times \mathbf{a}_3)}$$

$$\mathbf{b}_2 = 2\pi \frac{\mathbf{a}_3 \times \mathbf{a}_1}{\mathbf{a}_1 * (\mathbf{a}_2 \times \mathbf{a}_3)}$$

$$\mathbf{b}_3 = 2\pi \frac{\mathbf{a}_1 \times \mathbf{a}_2}{\mathbf{a}_1 * (\mathbf{a}_2 \times \mathbf{a}_3)},$$

yielding a discrete translation operation:

$$\mathbf{G} = m_1\mathbf{b}_1 + m_2\mathbf{b}_2 + m_3\mathbf{b}_3.$$

The direct and reciprocal lattice vectors satisfy the relation: $\mathbf{G} \cdot \mathbf{R} = 2\pi n$. The Wigner-Seitz primitive cell of the reciprocal lattice is known as the first Brillouin zone.

7.2.1 Fourier expansion

In quantum mechanics, a change in a basis used can considerably simplify computations. For example, a common basis change is from position space $\mathbf{r}\,|\psi\rangle$ into wave vector space or its crystal momentum $\mathbf{k}\,|\psi\rangle$ in section [3.7]. This section is meant to clarify how one can expand a function, such as a periodic cell part of an electron in a periodical solid (3.19), using another function in k-space.

Let's first consider transformation in a case of a general function that can be written using plane waves:

$$f(\mathbf{r}) = \int F(\mathbf{k}) e^{i\mathbf{k}\cdot\mathbf{r}} d\mathbf{k}. \tag{7.4}$$

This is known as the inverse Fourier transform from a reciprocal space function $F(\mathbf{k})$ into a real space function $f(\mathbf{r})$. Let us also assume that $f(\mathbf{r})$ obeys the periodicity for any Bravais lattice vector (7.3). We can now represent $f(\mathbf{r})$ as a Fourier expansion as a sum over the reciprocal lattice vectors $\mathbf{G}$:

$$f(\mathbf{r}) = \sum_{\mathbf{G}} h(\mathbf{G}) e^{i\mathbf{G}\cdot\mathbf{r}}, \tag{7.5}$$

where:

$$h(\mathbf{G}) = \frac{1}{\mathbf{a}_1(\mathbf{a}_2 \times \mathbf{a}_3)} \int_{\mathbf{\Omega}} f(\mathbf{r}) e^{-i\mathbf{G}\cdot\mathbf{r}} d^3\mathbf{r}.$$

$\Omega = \frac{1}{\mathbf{a}_1(\mathbf{a}_2 \times \mathbf{a}_3)}$ is the primitive unit cell volume.

References

[1] Feng Cheng & Xiuwei Li *Effects of In Situ Co or Ni Doping on the Photoelectrochemical Performance of Hematite Nanorod Arrays* Appl. Sci. 2020, 10, 3567

[2] Andebet Gedamu Tamirat, John Rick, Amare Aregahegn Dubale, Wei-Nien Su & Bing-Joe Hwang *Using hematite for photoelectrochemical water splitting: a review of current progress and challenges* Nanoscale Horiz., 2016, 1, 243

[3] Yongtao Menga, Xiao Zhangb, Wei-Hsuan Hungb, Junkai Hee ,Yi-Sheng Tsaid, Yun Kuangb, Michael J. Kenney, Jing-Jong Shyuef , Yijin Liug , Kevin H. Stoneg , Xueli Zhengh , Steven L. Suibe , Meng-Chang Lina , Yongye Liangc and Hongjie Daib *Highly active oxygen evolution integrated with efficient CO2 to CO electroreduction* PNAS November 26, 2019

[4] Jian Zhao, Song Xue, James Barber, Yiwei Zhou, Jie Menga & Xuebin Ke *An overview of Cu-based heterogeneous electrocatalysts for CO_2 reduction* J. Mater. Chem. A, 2020,8, 4700-4734

[5] Zuofeng Chen, Peng Kang, Ming-Tian Zhang, Brian R. Stonerb & Thomas J. Meyer *Cu(ii)/Cu(0) electrocatalyzed CO_2 and H_2O splitting* Energy Environ. Sci., 2013,6, 813-817

[6] Etienne Boutin and Marc Robert *Molecular Electrochemical Reduction of CO_2 beyond Two Electrons* Trends in Chemistry Volume 3, Issue 5, May 2021, Pages 359-372

[7] Congxin Xia, Yu Jia, Meng Tao, Qiming Zhang *Tuning the Band Gap of Hematite $\alpha - Fe_2O_3$ by Sulfur Doping* Physics Letters A 377 (2013) 1943–1947

[8] Yichun Yina, Xiwang Zhangb, Chenghua Sun *Transition-metal-doped Fe_2O_3 Nanoparticles for Oxygen Evolution Reaction* Progress in Natural Science: Materials International Volume 28, Issue 4, August 2018, Pages 430-436

[9] Akira Fujishima Kenichi Honda *Electrochemical Photolysis of Water at a Semiconductor Electrode* Nature volume 238, pages37–38 (1972)

[10] Jiliang Zhang, Vincent Wing-hei Lau, Chang-Zhong Liao, Kam Wa Wong, Gi-Hyeok Lee, Feng Zou, Chung-Kai Chang, Hwo-Shuenn Sheu Yong-Mook Kang *Controlling the Valence State of Cu Dopant in α-Fe_2O_3 Anodes: Effects on Crystal Structure and the Conversion Reactions with Alkali Ions* Chem. Mater. 2019, 31, 4, 1268–1279

[11] Suman, Surjeet Chahal, Ashok Kumar Parmod Kumar *Zn Doped $\alpha - Fe_2O_3$: An Efficient Material for UV Driven Photocatalysis and Electrical Conductivity* Crystals 2020, 10(4), 273

[12] W.R.W. Ahmad, M.H. Mamat, A.S. Zoolfakar, Z. Khusaimi, M.M. Yusof, A.S.Ismail, S.A. Saidi M. Rusop *The Effects of Sn-Doping on $\alpha - Fe_2O_3$ Nanostructures Properties* International Journal of Engineering Technology, 7 (3.11) (2018) 34-37

[13] Maria Vesna Nikolić, Dalibor L Sekulić, Milos Slankamenac Vladimir B. Pavlovic *Structural and Electrical Properties of Ti Doped -Fe2O3* Science of Sintering · September 2013

[14] William D. Chemelewski, Nathan T. Hahn, C. Buddie Mullins *Effect of Si Doping and Porosity on Hematite's ($\alpha - Fe_2O_3$) Photoelectrochemical Water Oxidation Performance* J. Phys. Chem. C 2012, 116, 8, 5255–5261

[15] Arnab Samanta, Sankar Das Subhra Jana *Doping of Ni in $\alpha - Fe_2O_3$ Nanoclews To Boost Oxygen Evolution Electrocatalysis* ACS Sustainable Chem. Eng. 2019, 7, 14, 12117–12124

[16] Huiyong Gong, Yurong He, Junqing Yin, Suyao Liu, Qing Peng, Chun-Fang Huo, Hong Wang, Yong Yang Xiao-Dong Wen *Electronic effects of transition metal dopants on Fe(100) and Fe_5C_2(100) surfaces for CO activation* Catal. Sci. Technol., 2020, 10, 2047

[17] Federico Franco, Clara Rettenmaier Hyo Sang Jeon Beatriz Roldan Cuenya *Transition metal-based catalysts for the electrochemical CO_2 reduction: from atoms and molecules to nanostructured materials* Chem. Soc. Rev., 2020,49, 6884-6946

[18] Jian Zhao, Song Xue, James Barber, Yiwei Zhou, Jie Menga Xuebin Ke *An overview of Cu-based heterogeneous electrocatalysts for CO_2 reduction* J. Mater. Chem. A, 2020,8, 4700-4734

[19] G. Hess, H. Froitzheim Ch. Baumgartner *The adsorption and catalytic decomposition of CO_2 on Fe(111) surfaces studied with high resolution EELS* Surface Science 331-333 (1995) 138-143

[20] Marco Favaro, Hai Xiao, Tao Cheng, William A. Goddard III, Junko Yano Ethan J. Crumlin *Subsurface oxide plays a critical role in CO_2 activation by Cu(111) surfaces to form chemisorbed CO_2 , the first step in reduction of CO_2* PNAS June 27, 2017 114 (26) 6706-6711

[21] Nicole J. Bernstein, Sneha A. Akhade Michael J. Janik *Density functional theory study of carbon dioxide electrochemical reduction on the Fe(100) surface* Phys. Chem. Chem. Phys., 2014, 16, 13708

[22] Cong Liu, Thomas R. Cundari, Angela K. Wilson *CO 2 Reduction on Transition Metal (Fe, Co, Ni, and Cu) Surfaces: In Comparison with Homogeneous Catalysis* J. Phys. Chem. C 2012, 116, 56815688

[23] Zan Kovac, Blaž Likozar, Matej Huš *Photocatalytic CO_2 Reduction: A Review of Ab Initio Mechanism, Kinetics, and Multiscale Modeling Simulations* ACS Catal. 2020, 10, 1498415007

[24] Nandha Kumar, Nicola Seriani Ralph Gebauer *DFT insights into electrocatalytic CO_2 reduction to methanol on $\alpha - Fe_2O_3(0001)$ surfaces* Phys. Chem. Chem. Phys., 2020, 22, 10819

[25] Kamil Czelej, Karol Cwieka, Tomasz Wejrzanowski, Piotr Spiewak Krzysztof Jan Kurzydlowski *Decomposition of activated CO_2 species on Ni(110): Role of surface diffusion in the reaction mechanism* PNAS June 27, 2017 114 (26) 6706-6711

[26] Nicole J. Bernstein, Sneha A. Akhade Michael J. Janik *Density functional theory study of carbon dioxide electrochemical reduction on the Fe(100) surface* Cite this: Phys. Chem. Chem. Phys., 2014, 16, 13708

[27] Ayoung Bak, Sung Kyu Choi, & Hyunwoong Park *Photoelectrochemical Performances of Hematite ($\alpha - Fe_2O_3$) Films Doped with Various Metals* Bull. Korean Chem. Soc., 36: 1487-1494 (2015)

[28] Charanjeet Singh, S. Bindra Narang, I.S. Hudiara, Yang Bai & Koledintseva Marina *Hysteresis analysis of Co–Ti substituted M-type Ba–Sr hexagonal ferrite* Materials Letters 63 (2009) 1921–1924

[29] SP. Keerthana, R. Yuvakkumar, G. Ravi, P. Kumar, Mohamed Soliman Elshikh, Hussein H. Alkhamis, Abdulwahed F. Alrefaei & Dhayalan Velauthapillai *A strategy to enhance the photocatalytic efficiency of $\alpha - Fe_2O_3$* Chemosphere 270 (2021) 129498

[30] Teng Lva, Wei Wenga, Jing Zhoub, Dong Gub, & Wei Xiaoa *Effects of K and Mn promoters over Fe_2O_3 on Fischer–Tropsch synthesis* Journal of Energy Chemistry Volume 47, August 2020, Pages 118-127

[31] Yulan Zhang, Longlong Ma, Tiejun Wang & Xinjun Li *MnO2 coated Fe_2O_3 spindles designed for production of C_{5+} hydrocarbons in Fischer–Tropsch synthesis* Fuel Volume 177, 1 August 2016, Pages 197-205

[32] Daniel Bahamon, Malathe Khalil, Abderrezak Belabbes, Yasser Alwahedi, Lourdes F. Vega & Kyriaki Polychronopoulou *A DFT study of the adsorption energy and electronic interactions of the SO_2 molecule on a CoP hydrotreating catalyst* RSC Adv., 2021,11, 2947-2957

[33] Xin Wei , Chaofang Dong , Zhanghua Chen , Kui Xiao & Xiaogang Li *A DFT study of the adsorption of O_2 and H_2O on Al(111) surfaces* RSC Adv., 2016, 6, 56303-56312

[34] N. W. Ashcroft a& N. D. Mermin *Solid State Physics* Saunders College Publishing, Philadelphia, PA, 1976

[35] John P. Perdew, Kieron Burke & Matthias Ernzerhof *Generalized Gradient Approximation Made Simple* Phys. Rev. Lett. 78, 1396 (1997)

[36] John P. Perdew & Yue Wang *Accurate and simple analytic representation of the electron-gas correlation energy* Phys. Rev. B 98, 079904 (2018)

[37] Yu Meng, Xing-Wu Liu, Chun-Fang Huo, Wen-Ping Guo, Dong-Bo Cao, Qing Peng, Albert Dearden, Xavier Gonze, Yong Yang, Jianguo Wang, Haijun Jiao, Yongwang Li & Xiao-Dong Wen *When Density Functional Approximations Meet Iron Oxides* J. Chem. Theory Comput. 2016, 12, 10, 5132–5144

[38] A. Rohrbach, J. Hafner, & G. Kresse *Ab initio study of the (0001) surfaces of hematite and chromia: Influence of strong electronic correlations* Phys. Rev. B 70, 125426

[39] *Materials Project* https://materialsproject.org/

[40] Hendrik J. Monkhorst & James D. Pack *Special points for Brillouin-zone integrations* Phys. rev. B, Volume 13, number 12, (1976)

[41] P. E. Blöchl *Projector augmented-wave method* Phys. Rev. B 50, 17953 (1994)

[42] G. Kresse & D. Joubert *From ultrasoft pseudopotentials to the projector augmented-wave method* Phys. Rev. B 59, 1758 (1999)

[43] S. L. Dudarev, G. A. Botton, S. Y. Savrasov, C. J. Humphreys & A. P. Sutton *Electron-energy-loss spectra and the structural stability of nickel oxide: An LSDA+U study* Phys. Rev. B 57, 1505 (1998)

[44] Vladimir I. Anisimov, Jan Zaanen & Ole K. Andersen *Band theory and Mott insulators: Hubbard U instead of Stoner I* Phys. Rev. B 44, 943 (1991)

[45] P. Hohenberg & W. Kohn *Inhomogeneous Electron Gas* Phys. Rev. 136, B864 (1964)

[46] W. Kohn *Nobel Lecture: Electronic structure of matter—wave functions and density functionals* Rev. Mod. Phys. 71, 1253 (1999)

[47] Richard F. W. Bader *Atoms in Molecules - A Quantum Theory* Oxford University Press, Oxford, 1990

[48] Graeme Henkelman, Andri Arnaldsson Hannes Jonsson *A fast and robust algorithm for Bader decomposition of charge density* Computational Materials Science 36 (2006) 354–360

[49] *Visualization for Electronic ans Structural Analysis: VESTA software* https://jp-minerals.org/vesta/en/

[50] Andri Arnaldsson, Wenjie Tang, Sam Chill, Wenrui Chai, Ryan Anselm, & Graeme Henkelman *Code: Bader Charge Analysis* http://theory.cm.utexas.edu/henkelman/code/bader/
The University of Texas at Austin

[51] *The materials project* https://materialsproject.org/
Initial Fe_2O_3 structure:

https://materialsproject.org/materials/mp-24972/
Hubbard U correction:
https://docs.materialsproject.org/methodology/gga-plus-u/

[52] S. Assa Aravindh, Wei Cao, Matti Alataloa, Marko Huttulaa & Jukka Kömi *Adsorption of CO_2 on the ω-Fe (0001) surface: insights from density functional theory* RSC Adv., 2021, 11, 6825-6830

[53] P. Fulde *Electron Correlations in Molecules and Solids* Springer, 1995

[54] E. Blanca, C. Rodriguez, J. Shitu & D. Novikov, *Degree of localization of the exchange-correlation hole and its influence on the ground-state(structural and magnetic) properties of d metals* J. Phys Condens. Matter 13, 9463 (2001)

[55] Abhishek Kumar Mishra, Alberto Roldan, & Nora H. de Leeuw *CuO Surfaces and CO_2 Activation: A Dispersion-Corrected DFT+U Study* J. Phys. Chem. C 2016, 120, 4, 2198–2214

[56] Dong-Bo Cao, Yong-Wang Li, Jianguo Wang & Haijun Jiao *CO_2 dissociation on Ni(2 1 1)* Surface Science 603 (2009) 2991–2998

[57] Junseok Lee, Dan C. Sorescu & Xingyi Deng *Electron-Induced Dissociation of CO_2 on TiO_2 (110)* J. Am. Chem. Soc. 2011, 133, 10066–10069

[58] Xuejing Liu, Lei Sun & Wei-Qiao Deng *Theoretical Investigation of CO_2 Adsorption and Dissociation on Low Index Surfaces of Transition Metals* J. Phys. Chem. C 2018, 122, 8306-8314

[59] David Santos-Carballal, Alberto Roldan, Nelson Y. Dzade & Nora H. de Leeuw *Reactivity of CO_2 on the surfaces of magnetite (Fe_3O_4), greigite (Fe_3S_4) and mackinawite (FeS)* Phil.Trans. R. Soc. A 376: 20170065 (2018)

[60] *Vienna Ab-initio Simulation Package* https://www.vasp.at/

[61] Peter E. Blöchl, O. Jepsen & O. K. Andersen *Improved tetrahedron method for Brillouin-zone integrations* Phys. Rev. B 49, 16223 – Published 15 June 1994

[62] W. H. Press, B. P. Flannery, S. A. Teukolsky & W. T. Vetterling *NUMERICAL RECIPES; The Art of Scientific Computing, Third Edition* Chapter 10, Cambridge University Press 2007

[63] Wenhao Sun & Gerbrand Ceder *Efficient creation and convergence of surface slabs* Surface Science 617 (2013) 53–59

[64] Natividad Gálvez Rodríguez, Vidal Barrón & José Torrent `Preparation and Properties of Hematite with Structural Phosphorus` Clays Clay Miner. 47, 375–385 (1999)

[65] Photo by Dave Dyet
https://www.freeimages.com/photographer/dyet-39194